

Transition Metal-Driven Variations in Structure, Magnetism, and Photocatalysis of Monoclinic M_3Se_4 ($M = Fe, Co, Ni$) Nanoparticles

Monika Ghalawat^{†,‡}, Inderjeet Chauhan^{†,‡}, Dinesh Singh^{†,‡}, Chinnakonda S.
Gopinath^{†,‡*}, Pankaj Poddar^{†,‡*}

[†]Physical & Materials Chemistry Division, CSIR-National Chemical Laboratory, Pune 411008, India

[‡]Academy of Scientific and Innovative Research (AcSIR), Sector 19, Kamla Nehru Nagar,
Ghaziabad, Uttar Pradesh- 201 002, India

ABSTRACT

The transition metal selenides (M_xSe_y) have gained attention for their unique physical and chemical properties, especially those associated with the transition metal (M). Despite advancements in synthesis, fabricating these selenides is challenging due to their complex stoichiometry and high asymmetry. One such system is monoclinic iron selenide (Fe_3Se_4), which can be used in permanent-magnet technologies and serve as a model system for understanding magnetism. This study focuses on fabricating monoclinic M_3Se_4 ($M = Fe, Co, or Ni$) compounds via thermal decomposition, examining how solution chemistry influences their morphology and properties. With a Curie temperature of about 322 K, Fe_3Se_4 is ferrimagnetic, whereas Co_3Se_4 and Ni_3Se_4 are paramagnetic between 5 and 300 K. The latter two compounds also show higher catalytic activity for hydrogen evolution in water splitting, with maximum H_2 -evolution rates of 1.01, 5.16, and 6.83 $mmol\ h^{-1}g^{-1}$ for Fe_3Se_4 , Co_3Se_4 , and Ni_3Se_4 , respectively.

Keywords: M_3Se_4 , transition metal selenides, thermal decomposition, magnetic and photocatalytic properties.

Corresponding Author

*E-mail: cs.gopinath@ncl.res.in, p.poddar@ncl.res.in.

INTRODUCTION

Although transition metal chalcogenides (TMCs) are thought to be exciting materials with extensive phase diagrams, their complexity, lack of control over stoichiometry, and shape make them more difficult to manage than oxides.¹⁻⁵ The properties of these materials— thermal and electronic (electrical, magnetic and optical)—are highly delicate to their crystalline phase, stoichiometry, shape, and size.⁶⁻¹¹ The surface-to-volume ratio further improves the tunability of chemical and physical properties due to nano-dimensionality. Nanoscale phenomena

provide an explanation for many of nature's wonders. A key challenge is controlling TMC phase formation chemistry. Transition metal selenides (M_xSe_y) are of special importance because of their electrical and thermal properties, which are determined by the transition metal (M), M-Se ratio, and crystallinity.^{12–16} For applications in magnetic materials over some other materials, like magnetic read-heads, ferrofluids, high-density memory storage using magnetic media, or the growing significance of magnetic nanoparticles (NPs) in biomagnetic applications, precise control over the elemental ratio, size, shape, crystallinity, and assembly of NPs is essential because even small changes in these parameters have a comparatively greater impact on the applications.^{17–24}

The Fe-Se system comprises four stable phases: orthorhombic $FeSe_2$, monoclinic Fe_3Se_4 , hexagonal Fe_7Se_8 , and tetragonal β - $FeSe$. In previous reports^{7,25}, we examined the intricacies of phase diagrams and stoichiometry in this system. Among four phases, Fe_3Se_4 exhibits unique ferrimagnetic properties due to ordered iron vacancies in alternating layers—in each layer, both the number and distribution of vacancies are different.⁷ Ferrimagnetic ordering is thought to have its roots in the spins that are antiferromagnetically aligned in a plane next to ordered iron vacancies and ferromagnetically aligned inside each plane along the c-axis.^{7,26,27}

Even in the absence of rare-earth or noble metal atoms, Fe_3Se_4 exhibits semi-hard magnetic characteristics below its Curie temperature at the nanoscale, making it a special material. Zhang et al.²⁷ found that when 90 kOe of the maximal external field was applied to nanoplatelets, the coercivity increased to around 40 kOe at 10 K from about 4 kOe at 300 K. Due to its monoclinic structure with ordered iron vacancies, Fe_3Se_4 exhibits a significant magnetocrystalline anisotropy $\sim 1.0 \times 10^7$ erg/cm³ at 10 K.²⁶ At 300 K, the energy product (BH_{max}) for Fe_3Se_4 nanorods was ~ 4.38 kG Oe, which was improved by Mn-doping in an applied magnetic field of over 85 kOe to 10.22 kG Oe.²⁸ Additionally, our recent work²⁹ highlights how controlling the shape of Fe_3Se_4 NPs affects magnetic properties, with coercivity and remanence increasing with size. The BH_{max} rises linearly with size, reaching 7.5 kG Oe for nanoplatelets and 7.1 kG Oe for nanorods at 300 K.

Due to the difficulty in fabricating highly asymmetric TMCs, the significant role of Fe in determining the magnetic characteristics of Fe_3Se_4 NPs has not yet been investigated. There have always been difficulties, curiosity, and possibilities related to the special and novel M-dependent characteristics that crystals exhibit. Therefore, to further comprehend the magnetic characteristics of Fe_3Se_4 , a thorough study of monoclinic M_3Se_4 compounds (M= Fe, Co, and

Ni) is intriguing and necessary. While Co_3Se_4 and Ni_3Se_4 are believed to be paramagnetic³⁰, this has not been experimentally verified. These compounds have also garnered attention for their high electrocatalytic activity in oxygen and hydrogen evolution reactions (OER and HER).^{31–34} However, due to the difficulty in the synthesis, there are no or very few reports on the nanoscale fabrication of single phase Co_3Se_4 . Furthermore, a binary photocatalyst $\text{Ni}_3\text{Se}_4@\text{CdS}$ has been created, and when exposed to visible light, it produces hydrogen at a rate of $7.57 \text{ mmol h}^{-1} \text{ g}^{-1}$.³⁵

M_3Se_4 (where $\text{M} = \text{Fe}, \text{Co},$ and Ni) is a transition metal selenide with a monoclinic crystal structure, $(\text{M}^{2+})_1(\text{M}^{3+})_2(\text{Se}^{2-})_4$. M_3Se_4 are crystallized in the monoclinic space group (SG)— $\text{I}2/\text{m}$ (Fe_3Se_4 and Ni_3Se_4) and $\text{C}2/\text{m}$ (Co_3Se_4) with distinct unit cell parameters (Figure 1). For Fe_3Se_4 ³⁶, the unit cell lattice parameters are $a=6.20 \text{ \AA}$, $b=3.54 \text{ \AA}$, and $c=11.28 \text{ \AA}$ [$\alpha=\gamma=90^\circ$, $\beta=91.807^\circ$] and for Ni_3Se_4 ³⁷ $a=6.19 \text{ \AA}$, $b=3.63 \text{ \AA}$, and $c=10.45 \text{ \AA}$ [$\alpha=\gamma=90^\circ$, $\beta=90.05^\circ$]. Whereas, for Co_3Se_4 ³⁸ the parameters are $a=12.10 \text{ \AA}$, $b=3.57 \text{ \AA}$, and $c=6.18 \text{ \AA}$ [$\alpha=\gamma=90^\circ$, $\beta=120.73^\circ$]. Each crystal structure has two geometrically different cation sites. For Fe_3Se_4 — $[\text{Fe}^{3+}]_A [\text{Fe}^{3+}\text{Fe}^{2+}]_B (\text{Se}^{2-})_4$: A sites are tetrahedrally coordinated by Se atoms and are occupied exclusively by Fe^{3+} cations, while B sites are octahedrally coordinated by Se atoms and are occupied by an equal number of Fe^{2+} and Fe^{3+} cations. For $(\text{Co/Ni})_3\text{Se}_4$ — $[(\text{Co/Ni})^{2+}]_A [((\text{Co/Ni})^{3+})_2]_B (\text{Se}^{2-})_4$: A sites are tetrahedrally coordinated by Se atoms and are occupied exclusively by $(\text{Co/Ni})^{2+}$ cations, while B sites are octahedrally coordinated by Se atoms and are occupied exclusively by $(\text{Co/Ni})^{3+}$ cations.

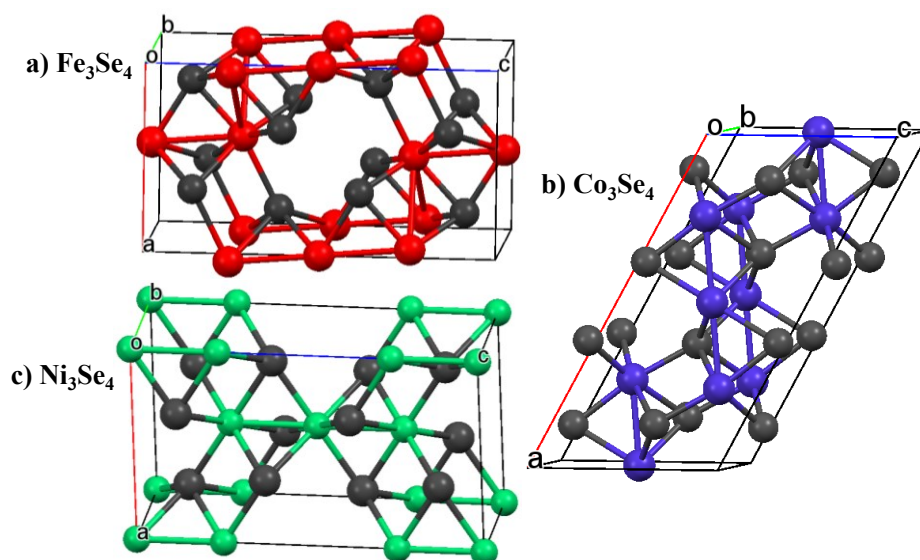


Figure 1. Schematic of the unit-cells of a) Fe_3Se_4 , b) Co_3Se_4 , and c) Ni_3Se_4 having monoclinic NiAs-type crystal structure. Red, blue, and green solid circles represent Fe, Co, and Ni cations. Dark grey solid circles represent Se anions.

This work utilizes thermal decomposition to achieve tunability of transition metals in complex M_3Se_4 compounds at the nanoscale. The thermal decomposition approach provides controlled synthesis, paving the way for regulated fabrication of other TMCs. Single-phase M_3Se_4 compounds have been synthesized and characterized using X-ray diffraction (XRD) and transmission electron microscopy (TEM). The study includes predictions of crystal habits using theoretical models and an exploration of the unique experimental morphologies. Thermogravimetric analysis (TGA) is used to assess decomposition behavior. Distinct magnetic and photocatalytic properties are observed with varying transition metals in monoclinic M_3Se_4 NPs, and the underlying reasons are discussed.

EXPERIMENTAL SECTION

Materials

Iron (III) acetylacetonate [$Fe(acac)_3$; 99.99%], cobalt (III) acetylacetonate [$Co(acac)_3$; 99.99%], nickel (II) acetylacetonate [$Ni(acac)_2$; 95%], selenium powder [Se; 99.99%], and oleylamine [OLA; 70%] were purchased from Sigma-Aldrich chemicals. All chemicals were used without further purification.

Thermal Decomposition Based Synthesis of M_3Se_4 Compounds

A one-pot thermal decomposition approach was employed to create monoclinic M_3Se_4 compounds. Starting with Fe_3Se_4 NPs as a reference²⁹, Co_3Se_4 and Ni_3Se_4 NPs were synthesized under identical conditions, differing only in the transition metal precursor. In each reaction, 1.5 mmol of metal acetylacetonate [0.53 g for $Fe(acac)_3$ and $Co(acac)_3$; 0.38 g for $Ni(acac)_2$] and 2 mmol of Se powder [0.158 g] were used. These precursors were dissolved in 15 mL of oleylamine (OLA) in a 100 mL round-bottom flask under nitrogen at 30 °C. The temperature was increased from 30 °C to 120 °C, held for 30 minutes, then ramped to 200 °C at 2 °C/min and further to 330 °C at 5 °C/min, where it was maintained for 60 minutes. A thermometer was inserted inside the RB-flask for all reactions to ensure temperature stability within ± 2.0 °C. After cooling the reaction to room temperature (RT), the samples were rinsed with 20 mL of 2-propanol, centrifuged, and rewashed with 15 mL of n-hexane and 10 mL of 2-propanol. The resulting precipitate was dried in a vacuum at RT, afterwards utilized for further analysis.

Synthesis of M_3Se_4 /P25 composite

To investigate H_2 production activity, varying wt% of M_3Se_4 (M = Fe, Co, Ni) co-catalysts were loaded with titania (Degussa-P25) using the dry impregnation method.³⁹⁻⁴⁰ The necessary concentrations of P25 and M_3Se_4 NPs were separately dissolved in ethanol and sonicated for

15 minutes. Afterward, the M_3Se_4 solution was incorporated to the P25 solution and sonicated for another 30 minutes to ensure homogeneous dispersion before drying for 12 hours at 60 °C. Figure S1 shows the final composite color for each M_3Se_4 weight percentage.

Preparation of photocatalyst thin films over glass plates

A 1.25×3.75 cm² glass plate (Figure S1b) was first washed with soap solution, then sonicated with de-ionized (DI) water and acetone for 45 minutes (15 minutes each), stored at 65 °C for three hours, and then utilized to create thin films. The photocatalyst thin films were prepared over the glass plates using the drop casting technique, which did not require the inclusion of binders.³⁹⁻⁴⁰ To achieve a homogeneous dispersion of the catalyst, 1 mg of photocatalyst (P25 or M_3Se_4 /P25) was incorporated to 1 mL of ethanol and sonicated for 30 minutes. A 100 μ L micropipette was used to repeatedly drop-cast this catalyst dispersion onto the glass plate, and it was allowed to dry for 12 hours in the ambient conditions.

Evolution of H₂ Via Photocatalysis

In order to test the photo-catalytic hydrogen production capacity, one sun condition (100 mW/cm²) was generated with a 300 W Xe Lamp and AM 1.5 filter (Newport solar simulator) source used at room temperature. In particular, a round-bottom glass flask with a volume of 72 ml was utilized as a reactor for the hydrogen evolution reaction. In the 72 ml reactor, which included 10 ml of methanol as sacrificial agent and 30 ml distilled water, the catalyst glass plate was placed exactly as it had been made. Then, a photo-catalyst-filled round bottom flask was purged with N₂ to exclude any dissolved oxygen in the solution and head space of reactor and subsequently exposed to one sun irradiation conditions. The generated H₂ was measured with a gas chromatograph (Agilent 7890). GC (Gas Chromatograph, Agilent 7890A) measurements verified that the only product in the gas phase was hydrogen.

Characterization Techniques

Powder XRD measurements were conducted on a PANalytical X'PERT PRO instrument ($\lambda = 1.54$ Å) over a 2θ range of 10°-80°. The size, morphology, SAED, and lattice images were characterized using a FEI Tecnai T20 TEM operated at 200 keV. The powders were dispersed in n-hexane, drop-casted onto a carbon-coated copper TEM grid, and loaded into a single tilt sample holder. Mercury⁴¹ 4.0.0 software was used to draw the internal crystal structures and packing diagrams of the M_3Se_4 compounds (Fe_3Se_4 , Co_3Se_4 , and Ni_3Se_4) crystal using the reported crystallographic information with COD numbers 1527086³⁵, 9012803³⁷, and 9009245³⁶, respectively. The indexed morphologies predicted using Bravais Friedel Donnay

Harker (BFDH), and Hartman Perdok (HP) methods were drawn using the *WinXMorph*⁴² program. Thermal stability was assessed using a TGA SDT model Q600 of TA Instruments Inc. USA at a heating rate of 10 °C/min. Magnetic measurements were performed with a superconducting quantum interference device-based vibrating sample magnetometer (SQUID-VSM) manufactured by Quantum Design, Inc., San Diego, USA. The powder samples were precisely weighed and packed inside a plastic sample holder, which fits into a brass specimen holder provided by Quantum Design Inc. with a negligible contribution to the overall magnetic signal. The magnetization versus magnetic field (M–H) loops is collected at a rate of 50 Oe s⁻¹ in a field sweep from ± 60 kOe at the vibrating frequency of 40 Hz. The magnetization versus temperature (M–T) measurements was performed at a temperature sweep from 5 K to more than 300 K in a field of 100 Oe following standard field-cooled (FC) and zero-field cooled (ZFC) sequences. Catalyst materials and devices made were thoroughly characterized by various analytical methods. Diffuse reflectance UV-Vis measurement was carried by Shimadzu spectrophotometer (model-UV2550) with spectral grade BaSO₄ as a reference material. Hydrogen production was measured at zero potential in the wireless thin film configuration using one sun condition, as explained earlier.

RESULTS AND DISCUSSION

Structural and Morphological Investigations of M₃Se₄ compounds

Powder XRD was used to thoroughly examine the crystallinity and phase purity of the as-synthesised M₃Se₄ (where M=Fe, Co, and Ni) compounds. FullProf⁴³ software was then used to do the Reitveld refinement (Figure 2). The diffraction patterns showed no unidentified peaks, confirming the absence of secondary phases within the detection limits of the XRD technique. The patterns matched the reported standard diffraction data for Fe₃Se₄, Co₃Se₄, and Ni₃Se₄, with no ambiguous reflections. Table S1 presents the details of the refinement. Fe₃Se₄ XRD data is discussed in our previous work also.²⁹ The Scherrer^{44,45} method was used to determine the crystallite sizes along various planes that corresponded to the strongest diffraction peaks: 42 ± 3 nm (-112) and 35 ± 3 nm (202) for Fe₃Se₄, 8 ± 2 nm (002) and 7 ± 2 nm (202) for Co₃Se₄, and 19 ± 2 nm (-112) and 17 ± 2 nm (-114) for Ni₃Se₄ along mentioned planes. All of the M₃Se₄ compounds with the various SG and the computed unit cell lattice parameters, as listed in Table S1, crystallized in the monoclinic crystal structure.

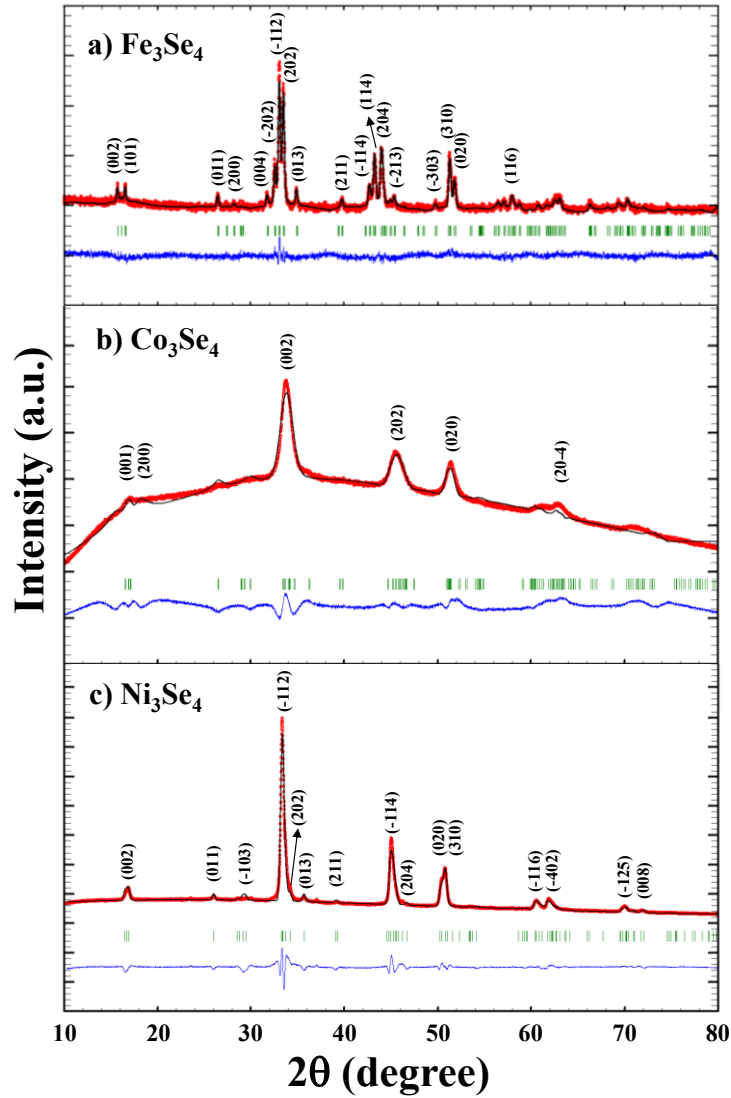


Figure 2. A comparison between experimentally obtained PXRD patterns (Observed Intensity I_{obs} vs. 2θ) of a) Fe_3Se_4 ²⁹, b) Co_3Se_4 , and c) Ni_3Se_4 (red lines) with calculated XRD curves (Calculated Intensity I_{cal} vs. 2θ) obtained using Rietveld refinement method (black line), $I_{\text{obs}} - I_{\text{cal}}$, difference curve (blue line), and Bragg positions (green vertical lines).

Even under identical reaction conditions, the atomic arrangement in monoclinic M_3Se_4 compounds varies as M changes from Fe to Co, resulting in distinct SGs. Atoms are organized in the $I2/m$ SG in Fe_3Se_4 and Ni_3Se_4 , however in Co_3Se_4 , they are placed in the $C2/m$ SG. Despite being members of the same category, the atomic configurations of the two SGs differ, which has an impact on the electrical characteristics and crystal shape that result. Buerger (1951) classified phase transitions as reconstructive (slow) or displacive (rapid) based on structural changes.⁴⁶ Reconstructive transitions, like graphite to diamond⁴⁷, involve significant structural changes and require high activation energy. Displacive transitions involve minor

bond distortions without breaking and occur readily with zero to minimal activation energy and cannot usually be prevented from occurring. Moreover, displacive transitions exhibit structural similarities. The two polymorphs have a symmetry relationship; the low-temperature polymorph has a low symmetry and is a subgroup of the high-temperature polymorph. Consequently, the displacive transitions are frequently seen in the same class of SGs. For instance, the C-centered clinopyroxenes $\text{LiScSi}_2\text{O}_6$ and ZnSiO_3 exhibit a displacive phase transition.⁴⁸ These transitions can only be detected using *in-situ* measurements. Displacive phase transitions are believed to occur in Fe_3Se_4 and Ni_3Se_4 , but they are too rapid for ex-situ characterization. In Co_3Se_4 , the reaction is incomplete, with atoms arranged in $C2/m$ SG, and no phase transition occurs due to gel formation. Their energy and time for the phase shift are insufficient. Diffraction peak broadening suggests larger particle sizes in Fe_3Se_4 and Ni_3Se_4 , while Co_3Se_4 particles remain small. Further microscopic analysis will provide additional insights into this phenomenon.

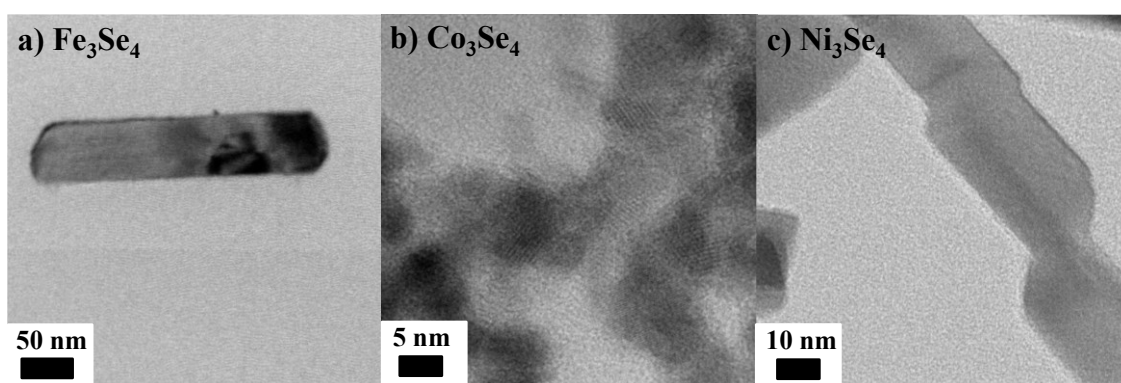


Figure 3. Typical TEM images of as-synthesized a) Fe_3Se_4 , b) Co_3Se_4 , and c) Ni_3Se_4 NPs (in the presence of OLA) show the rod-like features in Fe_3Se_4 and Ni_3Se_4 . In contrast, small quasi-spherical-like or random-shaped features are observed in Co_3Se_4 .

TEM analysis reveals that the as-synthesized M_3Se_4 compounds exhibit distinct morphologies: Fe_3Se_4 and Ni_3Se_4 form rod-like structures, while Co_3Se_4 appears as small quasi-spherical NPs (Figure 3). The NP shapes of Fe_3Se_4 and Ni_3Se_4 are similar, but Co_3Se_4 's morphology is markedly different. Scale bars indicate that all samples are within the nanometric range, with Fe_3Se_4 showing the fastest growth, producing large nanorods, followed by Ni_3Se_4 nanorods, and the smallest particles being the Co_3Se_4 quasi-spheres, despite identical reaction conditions.

All synthesized M_3Se_4 compounds underwent identical reactions, differing only by the metal acetylacetonate precursor used. As previously reported^{25,29}, metal-OLA and selenium-

OLA complexes are formed by metal and selenium precursors, respectively, and produce cations and anions. Compounds develop more quickly when there are more ions available. Selenium precursor reactivity will be similar to that covered in our earlier studies²⁵— Se-OLA complexes provide Se^{2-} . The decomposition behavior of metal precursors is crucial, influencing the rate of cation and compound formation. Multiple metal acetylacetonate's thermal breakdown was examined by Hoene et al.⁴⁹ The findings indicate that $\text{Fe}(\text{acac})_3$, $\text{Co}(\text{acac})_3$, and $\text{Ni}(\text{acac})_2$ start to break down at temperatures over 184 °C, 213 °C, and around 200 °C, respectively. $\text{Fe}(\text{acac})_3$ decomposes earliest, leading to the rapid growth of large Fe_3Se_4 nanorods. In contrast, $\text{Co}(\text{acac})_3$ decomposes at higher temperatures, resulting in smaller Co_3Se_4 nanoparticles. $\text{Ni}(\text{acac})_2$ falls in between, producing intermediate-sized Ni_3Se_4 nanorods. The metal precursor thus plays a key role in determining NP size in M_3Se_4 compounds.

After studying M_3Se_4 sizes, a detailed examination of the significant differences in M_3Se_4 shapes, as seen in TEM images, reveals that Fe_3Se_4 and Ni_3Se_4 NPs exhibit rod-like shapes, while Co_3Se_4 forms small quasi-spherical shapes under the same experimental conditions.

The theoretical analysis offers insights into these differences. Two primary approaches, Bravais Friedel Donnay Harker⁵⁰⁻⁵² (BFDH) and Hartman Perdok⁵³⁻⁵⁵ (HP), are typically used to predict crystal morphology. The specifics of the crystal habit calculations are covered in supporting information (Figure S2-S7 and Table S2-S3). The BFDH model, based on crystal parameters, shows that Co_3Se_4 has different crystal parameters and space groups (SG) compared to Fe_3Se_4 and Ni_3Se_4 , leading to a distinct crystal habit. In contrast, the HP model, which relies on bond energies, predicts minimal differences in morphology due to the similar bond energies across the compounds, with only slight directional variations. The variation in crystal parameters primarily influences the observed differences in NP shapes.

Materials behave more complexly in real-life reactions than they do in theoretically simplified models considering the effect of outside variables. Figure S8 illustrates the morphology of Fe_3Se_4 in both experimental and theoretical circumstances. According to both theoretical models, Fe_3Se_4 has a rod-like crystal habit, with the longitudinal sides being formed by the (001), (101), and (-101) planes. This prediction aligns with the observed experimental Fe_3Se_4 nanorods, which display lattice fringes at 5.6 Å and 2.6 Å corresponding to (002) and (202) planes on the longitudinal sides, confirming the rod-like shape. Our earlier study also discusses Fe_3Se_4 TEM observations in detail.^{7,25,29} In conclusion, the theoretical and experimental morphologies are consistent under the given reaction conditions.

In contrast, the crystal habit of Co_3Se_4 predicted by the BFDH and HP models differs significantly— Figure S9 illustrates the BFDH's rectangular-box shape and the HP model's compact cylindrical shape. Experimentally, Co_3Se_4 NPs are observed as small quasi-spherical shapes with (200) and (400) planes with lattice fringes at 5.2 Å and 2.6 Å. The Co_3Se_4 has only begun its formation process under our reaction conditions, resulting in very tiny NPs in comparison to other M_3Se_4 . When the reaction has started, the crystallographic model will dominate the crystal shape at low energy. Later, depending on the reaction environment, bond energy theories will also play a significant role. Since the number of intermolecular interactions in a crystal increases with its face area.⁵⁶ As a result, the growth rate increases in that direction, which in turn leads to a decrease in MI, and vice versa. As the (100) planes in Co_3Se_4 have a smaller facial area, interaction and growth in this face occur more slowly, leading to a greater MI of (100). Thus, at the initial stage of reactions, the crystallographic morphology dominates; consequently, with (200) and (400) planes on the upper side, the observed Co_3Se_4 NPs have a quasi-spherical form and are close to the BFDH model.

The morphology of the Ni_3Se_4 compound closely resembles that of Fe_3Se_4 , both theoretically and experimentally. Ni_3Se_4 shares the rod-like characteristics of (001), (101), and (-101) on the longitudinal sides according to both theoretical models, as was previously mentioned. Furthermore, as seen in Figure S10, the synthesized Ni_3Se_4 NPs are likewise shaped like a rod, with a 2.6 Å lattice fringe space in the (202) plane on the longitudinal side, which is fairly comparable to that of Fe_3Se_4 . In summary, since both theoretical models predict a rod-like morphology for Ni_3Se_4 , the experimental results align closely with these predictions, just as they do for Fe_3Se_4 .

Therefore, after taking into account the crystal habits of M_3Se_4 as well as the thermal decomposition of metal acetylacetonate, it is appropriate to conclude that, in the case of Fe_3Se_4 , the longer reaction time resulted in a largest-size rod shape NPs, whereas in the instance of Co_3Se_4 , the reaction barely began and produced small particles with a crystallographic crystal habit. Between these two extreme circumstances, Ni_3Se_4 has a rod-like shape but is smaller in size than Fe_3Se_4 .

Thermal Study

To investigate the decomposition behaviour of the as-synthesised NPs, the TGA of M_3Se_4 NPs was performed under a flowing nitrogen environment by heating the specimens over 25 °C to 1000 °C at a rate of 10 °C/min. Every sample exhibited an independent weight-loss tendency, illustrated in Figure S11. For Fe_3Se_4 , Co_3Se_4 , and Ni_3Se_4 , the weight loss was 3%, 15%, and

5%, respectively, with the initial step (<460 °C) being associated with the loss of organic particles (evaporation of capped OLA). The second step was devoted to the breakdown of M_3Se_4 , which begins at temperatures over 700 °C (weight loss ~4%, 20%, and 8%) and progressively drops to temperatures up to 1000 °C, with perceived (cumulative) weight loss of ~20%, 43%, and 32%, respectively. Here, the M_3Se_4 compounds decomposed into another $M_{1-x}Se$ -based molecule, which was followed by further decomposition. Fe_3Se_4 TGA data is covered in our previous work also²⁵.

Significant Impact of M on Magnetic Properties at Nanoscales in Monoclinic M_3Se_4 Compounds

Using SQUID-VSM, the impact of transition metals (M) on the nanoscale magnetic characteristics of M_3Se_4 compounds was evaluated. The Fe_3Se_4 magnetic properties are taken from our previous work²⁹. Figure 4 presents the temperature-dependent magnetization (M-T) curves for M_3Se_4 NPs in zero-field cooling (ZFC) and field cooling (FC) modes with an applied magnetic field of 100 Oe. For Fe_3Se_4 (Figure 4a), the M-T curve reveals a bifurcation below 330 K and a Curie transition temperature of ~322 K, indicating a ferrimagnetic phase below this temperature. Co_3Se_4 and Ni_3Se_4 (Figures 4b and 4c) show overlapping ZFC and FC curves across the entire temperature range (5K to more than 300 K), suggesting paramagnetic behavior with magnetic transition temperatures below the measurement range. Figure S12 further demonstrates that the magnetic susceptibility of both Co_3Se_4 and Ni_3Se_4 decreases with increasing temperature. The inverse of the magnetic susceptibility plot reveals that the extrapolation to zero temperature fails to obey the Curie Law. Instead, both the samples follow the Curie-Weiss Law as intercepts are above 0 K.⁵⁷

The magnetic field-dependent magnetization (M-H) of M_3Se_4 NPs was analyzed at 300 K and 10 K to explore their magnetic behavior. As previously reported^{27,29}, Figure 5a displays the hysteresis loops with typical non-linear behavior indicative of the ferrimagnetic nature of Fe_3Se_4 NPs at 300 K. In line with earlier research²⁶⁻²⁸, the magnetization remains unsaturated even at the maximum applied field of 60 kOe where the extremely high anisotropy field or the system's noncollinear spins prevented saturation even at 90 kOe. At 300 K, the coercivity (H_C) and remanence magnetization (M_R) values are 2.3 kOe and 2 emu/g, respectively, as shown in the inset of Figure 5a. At 10 K, the M-H curve remains unsaturated at 60 kOe (Figure 5a'), with coercivity values increasing significantly to 35.5 kOe—nearly 30 times greater than at 300 K—because of things like ferrimagnetism, an increase in total effective magnetic anisotropy, and a decrease in the thermal activation energy that gives up more and more spins

to orient in the field direction.²⁹ Additionally, at 10 K, the M_R increases from 2 emu/g at 300 K to 7.6 emu/g.

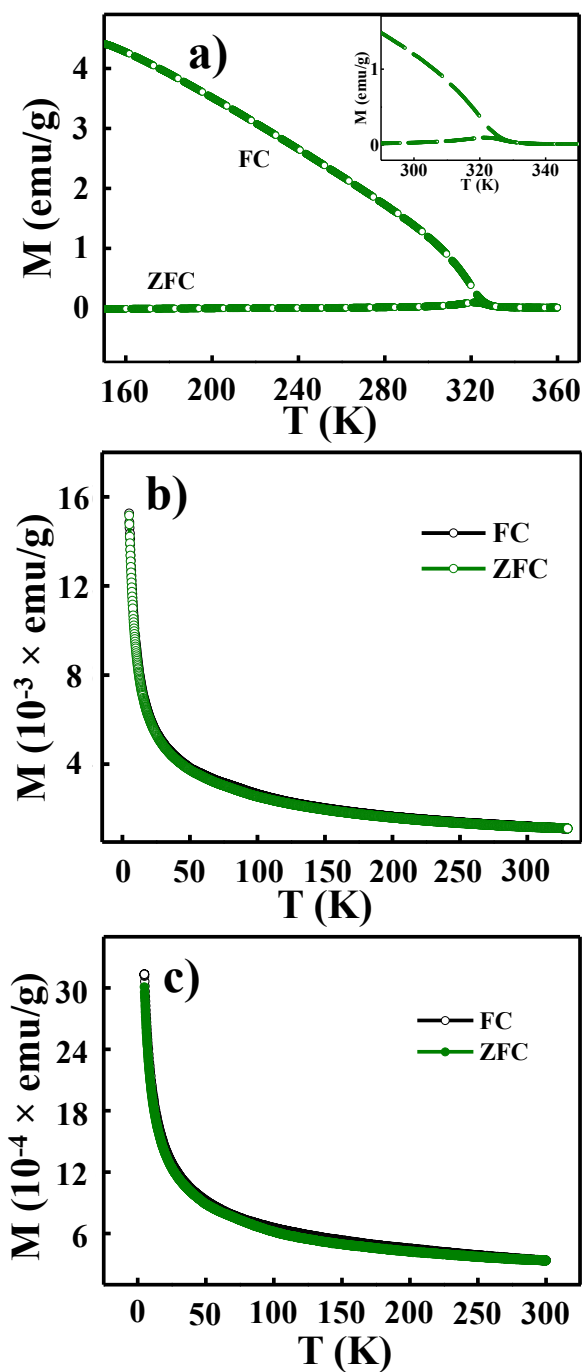


Figure 4. Comparison of magnetization versus temperature curves (in ZFC and FC modes) for all the as-synthesized M_3Se_4 NPs. a) to c) curves correspond to the samples— Fe_3Se_4 ²⁹, Co_3Se_4 , and Ni_3Se_4 , respectively, in the applied magnetic field of 100 Oe.

In contrast to Fe_3Se_4 , both Co_3Se_4 and Ni_3Se_4 exhibit linear M-H curves at 300 K, indicating a paramagnetic nature, which persists at 10 K as shown in Figures 5b-c and 5b'-c'. As a result, these compounds exhibit paramagnetic behavior at both observed temperatures

(300 K and 10 K), with the magnetic transition occurring below 10 K. The magnetic properties of M_3Se_4 compounds with a monoclinic crystal structure vary significantly with the transition metal: Fe_3Se_4 is ferrimagnetic at both 300 K and 10 K, while Co_3Se_4 and Ni_3Se_4 remain paramagnetic across the same temperature range. While the magnetic transition temperature in Co_3Se_4 and Ni_3Se_4 is lower than the lowest measured temperature (5 K), the Curie transition temperature of Fe_3Se_4 is close to 322 K. The magnetic characteristics change significantly even if the transition metal is changed from Fe to Co/Ni in the same structure. The explanation for this intriguing discovery resides in the magnetic characteristics of M_3X_4 (where $M = Fe, Co$ or Ni , and $X = O, S$ or Se) compounds.

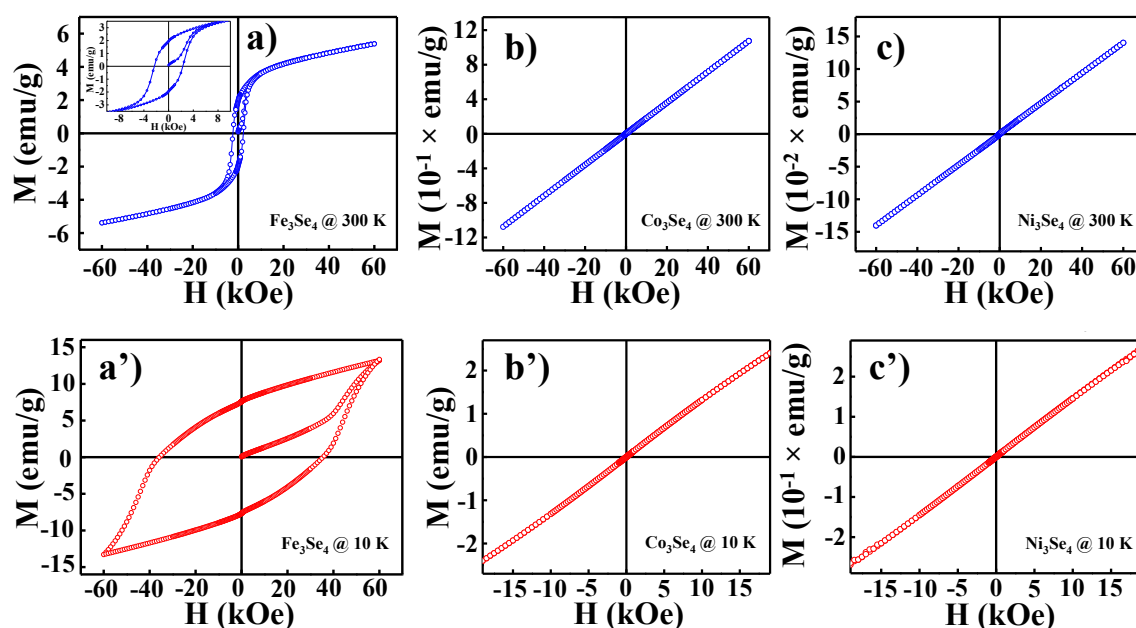


Figure 5. Magnetization vs. external magnetic field hysteresis loops at 300 K (blue curve) and 10 K (red curve) of M_3Se_4 NPs. a) to c) blue loops correspond to the samples— Fe_3Se_4 ²⁹, Co_3Se_4 , and Ni_3Se_4 , respectively at 300 K. a') to c') red loops correspond to the samples— Fe_3Se_4 ²⁹, Co_3Se_4 , and Ni_3Se_4 , respectively at 10 K.

The magnetic transition temperature (Curie or Neel temperature) of M_3X_4 compounds is displayed in Table S4.^{58–81} The key question is what will happen to magnetic characteristics if M (Fe, Co, or Ni) remains constant while X (O, S, or Se) changes, or vice versa.

1) Fe_3X_4 is used as a case study in order to comprehend the first point. The anion's atomic size grows as X shifts from O to S to Se, raising the lattice parameters and lowering the exchange interaction.⁸² The covalency effect and delocalization of 3D electrons also contribute to the reduction of the magnetic moment.⁸³ Overall, as X 's atomic size increases, magnetization decreases. As a result, when X 's atomic size increases, the thermal energy required to randomly

orient the magnetic spins reduces, and thus magnetic transition temperature reduces from O to Se. The Curie temperature reduces from ~ 858 K for Fe_3O_4 ⁵⁸⁻⁶² to ~ 314 K for Fe_3Se_4 .^{27,80}

2) In the second point, maintaining X constant and changing the M— M_3O_4 is used as a case study. The structure of Fe_3O_4 is inverted spinel. Fe^{2+} is diamagnetic as it is octahedral, having no unpaired electrons (t_{2g}^6). The arrangement of atoms in Fe_3O_4 compounds results in ferrimagnetism because Fe^{3+} is both tetrahedral ($e^2 t_2^3$) and octahedral ($t_{2g}^3 e_g^2$), with five unpaired electrons each, giving rise to a high magnetic moment.^{84,85} The normal spinel structure is occupied by the other two components, Co_3O_4 and Ni_3O_4 .⁸⁶⁻⁸⁹ The Co^{3+} in $\text{Co}_3\text{O}_4[\text{Co}^{2+}(\text{Co}^{3+})_2\text{O}_4]$ is in the octahedral state and has no unpaired electrons (low spin: t_{2g}^6), it possesses no magnetic moments. While, the Co^{2+} is in a tetrahedral configuration (high spin: $e^4 t_2^3$) and has a $3.26 \mu_B$ magnetic moment at 4.2 K. As a result, only Co^{2+} participates to the magnetism of the Co_3O_4 , which results in antiferromagnetic (AFM) behavior with a low Neel temperature (~ 40 K). As the overall magnetic moment is very small and only a small amount of thermal energy is required to randomly orient the magnetic moments.⁶³ In Ni_3O_4 , Ni^{2+} is in a tetrahedral state (high spin: $e^4 t_2^4$), and Ni^{3+} is in an octahedral state (low spin: $t_{2g}^6 e_g^1$). As both cations have unpaired electrons and are positioned so that each layer's total magnetization varies in magnitude, results in a ferrimagnetic nature with a Curie temperature of close to 808 K.⁶⁴⁻⁶⁸ The existence of more unpaired electrons in two types of Ni ions causes Ni_3O_4 to have more resultant magnetization than Co_3O_4 , which means that the magnetic transition temperature will be much greater in Ni_3O_4 compared to Co_3O_4 . As each Fe^{3+} has five unpaired electrons, the resulting magnetization is quite strong in the case of Fe_3O_4 , which also results in a high Curie temperature (~ 858 K).⁵⁸⁻⁶²

Combining these insights, we can address the behavior of M_3Se_4 compounds. Since the magnitude of the octahedral crystal field stabilizing energy reduces with increasing donor atom size. Thus, the Co and Ni ions move towards high spin states as the compounds transition from $(\text{Co}/\text{Ni})_3\text{O}_4$ to $(\text{Co}/\text{Ni})_3\text{Se}_4$. The exchange interaction declines from $\text{O} \rightarrow \text{S} \rightarrow \text{Se}$, resulting in a drop in total magnetization and magnetic transition temperature (as seen in Fe_3X_4 —the magnetic transition temperature reduces from O to Se). Some research on Co-based compounds has shown that Co_3S_4 is a temperature-independent paramagnetic⁷⁵, while other studies assert that it possesses an antiferromagnetic with a Neel temperature of about 58 K.^{76,77} Consequently, it is appropriate to draw the conclusion that magnetization has either reduced or remained relatively constant from O to S in Co-based compounds. Now when we move from S to Se, the exchange interaction decreases even more, lowering the magnetization in the instance of

Co₃Se₄ to the point where the magnetic transition temperature falls below the detection limits. In the case of Ni-based compounds, it significantly drops from 808 K⁶⁴⁻⁶⁸ (Ni₃O₄) to about 20 K^{78,79} for Ni₃S₄ and then falls below the detection limit for Ni₃Se₄. The magnetic transition temperature in Co₃Se₄ and Ni₃Se₄ is therefore below the lower limit of the measurement temperature.

M's Effect on Photocatalytic Properties as a Cocatalyst in Monoclinic M₃Se₄ Compounds

The XRD patterns of each catalyst are shown in Figure S13, which further confirms the catalysts' phase structure as manufactured. It displays clear diffraction peaks, proving that TiO₂ and M₃Se₄ were effectively synthesized and that, within the bounds of laboratory XRD, they have acceptable crystallinity. In case of Fe/Ni₃Se₄ cocatalyst, XRD reveals small shoulder and peaks above 5 wt% of corresponding cocatalyst.

The UV-vis spectroscopy and Tauc plot were used to investigate the samples' optical characteristics and band gap structure.⁹⁰ Figure S14 a-c shows that both pure TiO₂ and M₃Se₄/TiO₂ samples exhibit a significant absorption in the UV light region, which is characteristic of TiO₂. The as-prepared M₃Se₄ materials display a strong absorption in the entire visible light region, which corresponds to their narrow band gap. Green curve observed for 5% Ni₃Se₄ integrated TiO₂ suggests the visible light absorption from orange-red region of visible light spectrum and below. Similarly, blue curve associated with Co₃Se₄ also indicating the light absorption for almost the entire visible range. While red curve associated with Fe₃Se₄ hinting the light absorption to extend into NIR with possibly smaller band gap than the other two counterparts. Indeed, all the three chalcogenides are known to be a low band-gap semiconductors and visible light absorption is easily facilitated. In view of visible light absorption, they also act as visible light absorption component after integration with TiO₂, apart from the role of co-catalyst. Nonetheless, large amount of co-catalyst loading on TiO₂ itself would prevent efficient light absorption, which is counterproductive to light to charge carrier generation applications, such as photocatalysis. The samples' band gap energy was assessed using the Tauc plots⁹⁰, which were produced using the formulas of

$$[F(R).hv]^n = A (hv - E_g) \text{ and } [\alpha hv]^n = A (hv - E_g)$$

(A is a constant, n = 2 for the direct band gap semiconductor).

The linear extrapolation of Tauc plots yielded a band gap energy of approximately 3.24 eV for TiO₂ (Figure S14a'-c'). However, 5 wt % chalcogenide integrated TiO₂ shows a comparable band-gap between 3.1 and 3.2 eV, indicating that they are comparable.

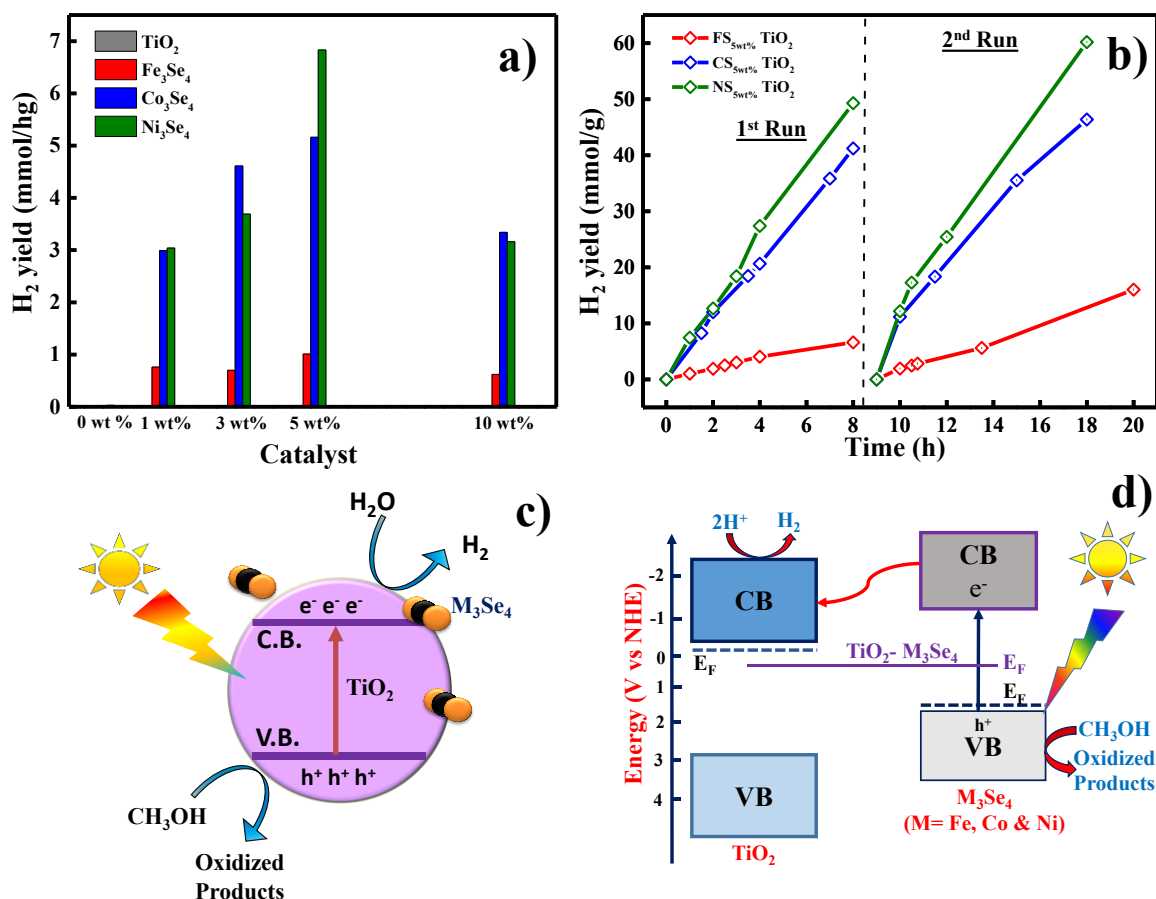


Figure 6. a) Photocatalytic solar hydrogen production with TiO₂ and M₃Se₄ as a co-catalyst for 4 h with different wt% of cocatalyst. b) Time dependent and cumulative photocatalytic hydrogen evolution of M₃Se₄ (5wt%)-TiO₂ catalysts. Cycling test of M₃Se₄ (5wt%)-TiO₂ for the photocatalytic H₂ evolution under one sun irradiation conditions. After 1st run of 8 h, the reactor was evacuated to remove the H₂ generated before the commencement of irradiation for 2nd run. c-d) The proposed photocatalytic mechanism for hydrogen evolution water splitting under visible light irradiation.

Using methanol as the sacrificial reagent, the photo-catalytic activity of TiO₂ and M₃Se₄ (1 to 10 wt%)-TiO₂ samples was examined under visible light irradiation. As shown in Figure 6a, pure TiO₂ exhibited a very low photocatalytic activity with a meagre solar hydrogen production yield of 0.029 mmol h⁻¹g⁻¹ under one sun conditions. Following the combination of TiO₂ and M₃Se₄, the composite catalyst demonstrates more photocatalytic activity than with TiO₂ alone. This is due to two reasons, namely, significant visible light absorption by co-catalyst which enhances the generation of electron-hole pairs. Second the heterojunctions created between TiO₂ and M₃Se₄ helps to rapidly separate the electron-hole pair generated, and the electrons are transferred to the CB of TiO₂. Additionally, this significantly reduces the ability of photo-

produced charge carriers to recombine. From $M_3Se_4(1 \text{ wt\%})-TiO_2$ to $M_3Se_4(5 \text{ wt\%})-TiO_2$, the H_2 generation activity progressively rises and then falls for all three chalcogenides. Therefore, the optimal loading quantity of M_3Se_4 is 5 wt % and the highest H_2 -evolution values was 1.01, 5.16 and 6.83 $mmol \text{ h}^{-1}g^{-1}$ for Fe_3Se_4 , Co_3Se_4 and Ni_3Se_4 , respectively. It illustrates how the amount of M_3Se_4 that is loaded onto the surface of TiO_2 NPs is essential for increasing the samples' photo-catalytic water-splitting activity because too much M_3Se_4 may hinder the swift transfer of electrons.

It is appropriate to conclude that the effect of M in M_3Se_4 composition of co-catalysts is strong on the photocatalytic activity for H_2 evolution. The activity of bare TiO_2 NPs for photocatalytic H_2 evolution was found to be fairly low (Figure 6a). After adding M_3Se_4 as a cocatalyst the activity increased prominently. In case of Fe_3Se_4 as a cocatalyst, the highest achieved activity is 1.01 $mmol \text{ h}^{-1}g^{-1}$, while in case of other two cocatalysts, it is increasing 5 to 6 times greater than that of Fe_3Se_4 and nearly 180 to 235 times better than that of TiO_2 NPs. This manifests that the $Ni_3Se_4(5 \text{ wt\%})-TiO_2$ and $Co_3Se_4(5 \text{ wt\%})-TiO_2$ materials prepared by above mentioned process has a close contact between TiO_2 and co-catalyst. TEM results shown earlier indicate the possibility of integration of TiO_2 with Fe_3Se_4 is low, due to its large particle size than the other two chalcogenides; however, Co_3Se_4 and Ni_3Se_4 shows comparable particle size range. Additionally, the advantage of nanorod with the Ni_3Se_4 cannot be ignored, as it can interact with several TiO_2 particles. A careful analysis of results shown in Figure 6a suggests the hydrogen production per unit weight of co-catalyst is the highest with Ni_3Se_4 at 5 wt %, while the same is true with Co_3Se_4 at 5 wt %. Hence it may be concluded that both the co-catalysts are comparable in terms of activity, however due to rod-shape of Ni_3Se_4 , it shows slightly higher activity.

As demonstrated in Figure 6b, the photo-catalytic stability of the water-splitting process of $M_3Se_4(5 \text{ wt\%})-TiO_2$ samples was evaluated. Two cycles of the stability test were carried out. Figure 6b makes it evident that the $M_3Se_4(5 \text{ wt\%})-TiO_2$ catalyst sustains a high rate of hydrogen production per cycle, indicating that it has good stability. The primary reason for this is that the addition of M_3Se_4 as an electron promoter could continuously speed up the separation and transfer of photo-generated charge carriers on the surface of TiO_2 .

The photo-catalytic reaction process and electron transfer mechanism under visible light irradiation were hypothesized based on the aforementioned results, presented in Figure 6c-d. Irradiation with one sun conditions produces photo-induced electron-hole pairs on both TiO_2 . The rate of H_2 evolution for the TiO_2 without any co-catalyst was very low due to the fast recombination of photo-excited electron-hole pairs, despite the fact that the conduction

band (CB) potential of TiO_2 is more negative than the reduction potential of H^+/H_2 . When exposed to visible light, the electrons in the M_3Se_4 valence band (VB) became excited and swiftly moved to the CB position of TiO_2 . To effectively prevent photo-generated electron and hole recombination, M_3Se_4 particles were distributed on the surface of TiO_2 as a co-catalyst to speed up charge carrier separation and transfer; in other words, charge carrier recombination would be effectively prevented. Therefore, adding M_3Se_4 can improve the HER's active site and speed up electron transfer, increasing the composite catalyst's capacity to produce hydrogen. A large jump in solar hydrogen production after introduction of M_3Se_4 on TiO_2 underscores the integrated nature of the final photocatalyst composite. 200 times increase in activity with Ni_3Se_4 (5 wt%)- TiO_2 than TiO_2 underscores an efficient separation of charge carriers at the heterojunctions between the components in the former. This integration aspect necessarily shifts the Fermi level of the composite, which is different from the constituent components, and shown schematically in Figure 6d. This makes the electron transfer very facile and ultimately enhances the solar hydrogen production.

Further, these compounds are very promising in various scientific domains. Researchers are focusing more on these areas because Ni_3Se_4 is also a viable catalyst and Co_3Se_4 recently attracted a lot of attention due to its high OER values through electrocatalysis and photoelectrochemical water splitting.³¹⁻³⁵ The other characteristics of these pure as-synthesised chemicals will therefore be fascinating and crucial to investigate further in the future.

CONCLUSION

Transition metal selenides are difficult to fabricate, and it is more challenging to create compounds with more asymmetry. The thermal decomposition approach was used in this work to manufacture the M_3Se_4 compounds (where $\text{M} = \text{Fe}, \text{Co}, \text{or Ni}$) in a monoclinic crystal structure with unique SG, resulting in a variety of morphologies. The atoms of Co_3Se_4 are arranged in C2/m , whereas the SG of Fe_3Se_4 and Ni_3Se_4 is I2/m . It is most likely the displacive transition that causes the unique SG. Theoretical models (BFDH and HP) assist in the understanding of the observed varying morphologies. Additionally, the impact of transition metal (M) on the magnetic characteristics of M_3Se_4 NPs is also examined. The Curie temperature of the ferrimagnetic Fe_3Se_4 is close to 322 K. Co_3Se_4 and Ni_3Se_4 , on the other hand, are temperature-independent paramagnetic throughout the entire measurement temperature range (5 K to 300 K). In the latter two compounds, the magnetic transition temperature is so low that it cannot be detected within measurement limitations. However,

these compounds as a cocatalyst shows prominent activity. The optimal loading quantity of M_3Se_4 is 5 wt % and the maximum H_2 -evolution values were $1.01 \text{ mmol h}^{-1}\text{g}^{-1}$, $5.16 \text{ mmol h}^{-1}\text{g}^{-1}$ and $6.83 \text{ mmol h}^{-1}\text{g}^{-1}$ for Fe_3Se_4 , Co_3Se_4 and Ni_3Se_4 , respectively. The activity is 5 to 6 times higher than that of Fe_3Se_4 in other two compounds and almost 180 to 235 times better than that of TiO_2 NPs. Furthermore, the catalyst M_3Se_4 (5 wt%)- TiO_2 sustains a high rate of hydrogen generation per cycle, indicating that it has good stability. To sum up, the work offers a suitable technique for creating M_3Se_4 NPs with unique M that have a range of magnetic and catalytic characteristics. This approach can be expanded to include the majority of TMCs.

ASSOCIATED CONTENT

Supporting Information

Rietveld refinement, BFDH, HP, packing diagram of M_3Se_4 , magnetic properties, XRD and UV-vis of catalyst.

Conflict of Interest Statement

The author (M.G.) declares that there is no conflict of interest regarding the publication of this work. This research is part of the author's Ph.D. thesis, which has been submitted and is publicly available on the institute's website. The reference for the thesis is <https://dspace.ncl.res.in/xmlui/handle/20.500.12252/6067>; titled as "Physics of transition metal chalcogenides based on deeper investigation of their phase-diagram and crystal growth mechanism".

AUTHOR INFORMATION

Corresponding Author

*E-mail: cs.gopinath@ncl.res.in, p.poddar@ncl.res.in.

Orchid

Pankaj Poddar: [0000-0002-2273-588X](https://orcid.org/0000-0002-2273-588X)

Notes

The authors declare no competing financial interest.

ACKNOWLEDGMENTS

One of the authors—MG acknowledges the support from the University Grants Commission (UGC), India, for providing the Senior Research Fellowship (SRF).

REFERENCES

- (1) Matthews, P. D.; McNaughten, P. D.; Lewis, D. J.; O'Brien, P. Shining a Light on Transition Metal Chalcogenides for Sustainable Photovoltaics. *Chemical Science* **2017**, *8* (6), 4177–4187. <https://doi.org/10.1039/C7SC00642J>.
- (2) Jellinek, F. Transition Metal Chalcogenides. Relationship between Chemical Composition, Crystal Structure and Physical Properties. *Reactivity of Solids* **1988**, *5* (4), 323–339. [https://doi.org/10.1016/0168-7336\(88\)80031-7](https://doi.org/10.1016/0168-7336(88)80031-7).
- (3) Theerthagiri, J.; Karuppasamy, K.; Durai, G.; Rana, A.; Arunachalam, P.; Sangeetha, K.; Kuppusami, P.; Kim, H.-S. Recent Advances in Metal Chalcogenides (MX; X = S, Se) Nanostructures for Electrochemical Supercapacitor Applications: A Brief Review. *Nanomaterials* **2018**, *8* (4), 256. <https://doi.org/10.3390/nano8040256>.
- (4) Tremel, W.; Kleinke, H.; Derstroff, V.; Reisner, C. Transition Metal Chalcogenides: New Views on an Old Topic. *Journal of Alloys and Compounds* **1995**, *219* (1–2), 73–82. [https://doi.org/10.1016/0925-8388\(94\)05064-3](https://doi.org/10.1016/0925-8388(94)05064-3).
- (5) Nath, M.; Singh, H.; Saxena, A. Progress of Transition Metal Chalcogenides as Efficient Electrocatalysts for Energy Conversion. *Current Opinion in Electrochemistry* **2022**, *34*, 100993. <https://doi.org/10.1016/j.coelec.2022.100993>.
- (6) Shenoy, S.; Jang, E.; Park, T. J.; Gopinath, C. S.; Sridharan, K. Cadmium sulfide nanostructures: Influence of morphology on the photocatalytic degradation of erioglaucine and hydrogen generation. *Applied Surface Science* **2019**, *483*, 696–705. <https://doi.org/10.1016/j.apsusc.2019.04.018>.
- (7) Ghalawat, M.; Poddar, P. Remarkable Effect of Fe and Se Composition on Magnetic Properties—Comparative Study of the Fe–Se System at the Nanoscale. *The Journal of Physical Chemistry C* **2022**, *126* (9), 4655–4663. <https://doi.org/10.1021/acs.jpcc.1c10286>.
- (8) Chavali, M. S.; Nikolova, M. P. Metal Oxide Nanoparticles and Their Applications in Nanotechnology. *SN Applied Sciences* **2019**, *1* (6), 607. <https://doi.org/10.1007/s42452-019-0592-3>.
- (9) Mourdikoudis, S.; Pallares, R. M.; Thanh, N. T. K. Characterization Techniques for Nanoparticles: Comparison and Complementarity upon Studying Nanoparticle Properties. *Nanoscale* **2018**, *10* (27), 12871–12934. <https://doi.org/10.1039/C8NR02278J>.
- (10) Bajpai, H.; Patra, K. K.; Ranjan, R.; Nalajala, N.; Reddy, K. P.; Gopinath, C. S. Can Half-a-Monolayer of Pt Simulate Activity Like That of Bulk Pt? Solar Hydrogen Activity Demonstration with Quasi-artificial Leaf Device, *ACS Appl. Mater. Interfaces* **2020**, *12*, 30420–30430. <https://doi.org/10.1021/acsami.0c07431>.
- (11) Baig, N.; Kammakakam, I.; Falath, W. Nanomaterials: A Review of Synthesis Methods, Properties, Recent Progress, and Challenges. *Materials Advances* **2021**, *2* (6), 1821–1871. <https://doi.org/10.1039/D0MA00807A>.

- (12) Shinde, P. A.; Chodankar, N. R.; Abdelkareem, M. A.; Patil, S. J.; Han, Y.; Elsaied, K.; Olabi, A. G. All Transition Metal Selenide Composed High-Energy Solid-State Hybrid Supercapacitor. *Small* **2022**, *18* (20), 2200248. <https://doi.org/10.1002/sml.202200248>.
- (13) Zeng, C.; Dai, L.; Jin, Y.; Liu, J.; Zhang, Q.; Wang, H. Design Strategies toward Transition Metal Selenide-Based Catalysts for Electrochemical Water Splitting. *Sustainable Energy & Fuels* **2021**, *5* (5), 1347–1365. <https://doi.org/10.1039/D0SE01722A>.
- (14) Zhou, H.; Li, X.; Li, Y.; Zheng, M.; Pang, H. Applications of MxSey (M = Fe, Co, Ni) and Their Composites in Electrochemical Energy Storage and Conversion. *Nano-Micro Letters* **2019**, *11* (1), 40. <https://doi.org/10.1007/s40820-019-0272-2>.
- (15) Xia, B.; Gao, D.; Xue, D. Ferromagnetism of Two-Dimensional Transition Metal Chalcogenides: Both Theoretical and Experimental Investigations. *Nanoscale* **2021**, *13* (30), 12772–12787. <https://doi.org/10.1039/D1NR02967C>.
- (16) Lu, T.; Dong, S.; Zhang, C.; Zhang, L.; Cui, G. Fabrication of Transition Metal Selenides and Their Applications in Energy Storage. *Coordination Chemistry Reviews* **2017**, *332*, 75–99. <https://doi.org/10.1016/j.ccr.2016.11.005>.
- (17) Zhang, H.; Liu, Y.; Sun, S. Synthesis and Assembly of Magnetic Nanoparticles for Information and Energy Storage Applications. *Frontiers of Physics in China* **2010**, *5* (4), 347–356. <https://doi.org/10.1007/s11467-010-0104-9>.
- (18) Nisticò, R.; Cesano, F.; Garello, F. Magnetic Materials and Systems: Domain Structure Visualization and Other Characterization Techniques for the Application in the Materials Science and Biomedicine. *Inorganics (Basel)* **2020**, *8* (1), 6. <https://doi.org/10.3390/inorganics8010006>.
- (19) Colombo, M.; Carregal-Romero, S.; Casula, M. F.; Gutiérrez, L.; Morales, M. P.; Böhm, I. B.; Heverhagen, J. T.; Prosperi, D.; Parak, Wolfgang. J. Biological Applications of Magnetic Nanoparticles. *Chemical Society Reviews* **2012**, *41* (11), 4306. <https://doi.org/10.1039/c2cs15337h>.
- (20) Khan, I.; Saeed, K.; Khan, I. Nanoparticles: Properties, Applications and Toxicities. *Arabian Journal of Chemistry* **2019**, *12* (7), 908–931. <https://doi.org/10.1016/j.arabjc.2017.05.011>.
- (21) Ray, P. C. Size and Shape Dependent Second Order Nonlinear Optical Properties of Nanomaterials and Their Application in Biological and Chemical Sensing. *Chemical Reviews* **2010**, *110* (9), 5332–5365. <https://doi.org/10.1021/cr900335q>.
- (22) Sun, H.-L.; Shi, H.; Zhao, F.; Qi, L.; Gao, S. Shape-Dependent Magnetic Properties of Low-Dimensional Nanoscale Prussian Blue (PB) Analogue SmFe(CN)₆·4H₂O. *Chemical Communications* **2005**, No. 34, 4339. <https://doi.org/10.1039/b507240a>.
- (23) Oyarzún, S.; Tamion, A.; Tournus, F.; Dupuis, V.; Hillenkamp, M. Size Effects in the Magnetic Anisotropy of Embedded Cobalt Nanoparticles: From Shape to Surface. *Scientific Reports* **2015**, *5* (1), 14749. <https://doi.org/10.1038/srep14749>.

- (24) Jeevanandam, J.; Barhoum, A.; Chan, Y. S.; Dufresne, A.; Danquah, M. K. Review on Nanoparticles and Nanostructured Materials: History, Sources, Toxicity and Regulations. *Beilstein Journal of Nanotechnology* **2018**, *9*, 1050–1074. <https://doi.org/10.3762/bjnano.9.98>.
- (25) Ghalawat, M.; Poddar, P. Study of the Phase-Evolution Mechanism of an Fe–Se System at the Nanoscale: Optimization of Synthesis Conditions for the Isolation of Pure Phases and Their Controlled Growth. *Langmuir* **2020**, *36* (8), 2012–2022. <https://doi.org/10.1021/acs.langmuir.9b03643>.
- (26) Long, G.; Zhang, H.; Li, D.; Sabirianov, R.; Zhang, Z.; Zeng, H. Magnetic Anisotropy and Coercivity of Fe₃Se₄ Nanostructures. *Applied Physics Letters* **2011**, *99* (20), 202103. <https://doi.org/10.1063/1.3662388>.
- (27) Zhang, H.; Long, G.; Li, D.; Sabirianov, R.; Zeng, H. Fe₃Se₄ Nanostructures with Giant Coercivity Synthesized by Solution Chemistry. *Chemistry of Materials* **2011**, *23* (16), 3769–3774. <https://doi.org/10.1021/cm201610k>.
- (28) Sen Bishwas, M.; Das, R.; Poddar, P. Large Increase in the Energy Product of Fe₃Se₄ by Fe-Site Doping. *The Journal of Physical Chemistry C* **2014**, *118* (8), 4016–4022. <https://doi.org/10.1021/jp411956q>.
- (29) Ghalawat, M.; Poddar, P. Study of Growth Kinetics of Fe₃Se₄ Nanocrystallites and the Influence of Size and Shape Tunability on Their Magnetic Properties. *The Journal of Physical Chemistry C* **2021**, *125* (14), 7932–7943. <https://doi.org/10.1021/acs.jpcc.1c00389>.
- (30) Hayashi, A.; Imada, K.; Inoue, K.; Ueda, Y.; Kosuge, K. Phase Diagram of (M'_xM_{1-x})₃Se₄ (0 ≤ x ≤ 1) (M, M' = 3d-Transition Metal) Bull. Inst. Chem. Res., Kyoto Univ., 1986, *64*, 4. <http://hdl.handle.net/2433/77161>.
- (31) Li, W.; Gao, X.; Xiong, D.; Wei, F.; Song, W.-G.; Xu, J.; Liu, L. Hydrothermal Synthesis of Monolithic Co₃Se₄ Nanowire Electrodes for Oxygen Evolution and Overall Water Splitting with High Efficiency and Extraordinary Catalytic Stability. *Advanced Energy Materials* **2017**, *7* (17), 1602579. <https://doi.org/10.1002/aenm.201602579>.
- (32) Sim, Y.; John, J.; Surendran, S.; Moon, B.; Sim, U. Efficient Photoelectrochemical Water Splitting Reaction Using Electrodeposited Co₃Se₄ Catalyst. *Applied Sciences* **2018**, *9* (1), 16. <https://doi.org/10.3390/app9010016>.
- (33) Du, J.; Zou, Z.; Liu, C.; Xu, C. Hierarchical Fe-Doped Ni₃Se₄ Ultrathin Nanosheets as an Efficient Electrocatalyst for Oxygen Evolution Reaction. *Nanoscale* **2018**, *10* (11), 5163–5170. <https://doi.org/10.1039/C8NR00426A>.
- (34) Wu, P.; Sun, G.; Chen, Y.; Xu, W.; Zheng, H.; Xu, J.; Wang, L.; Peng, D.-L. MoSe₂-Ni₃Se₄ Hybrid Nanoelectrocatalysts and Their Enhanced Electrocatalytic Activity for Hydrogen Evolution Reaction. *Nanoscale Research Letters* **2020**, *15* (1), 132. <https://doi.org/10.1186/s11671-020-03368-z>.
- (35) Wang, H. Enhanced Effect of Ni₃Se₄ Modified CdS Nanorod for Efficient Hydrogen Production. *Catal Lett* **2020**, *150*, 849–860. <https://doi.org/10.1007/s10562-019-02976-4>.

- (36) Andresen, A. F.; van Laar, B.; Kvamme, E.; Ohlson, R.; Shimizu, A. The Magnetic Structure of Fe_3Se_4 . *Acta Chemica Scandinavica* **1970**, *24*, 2435–2439. <https://doi.org/10.3891/acta.chem.scand.24-2435>.
- (37) Hiller, J. E.; Wegener, W. Untersuchungen im system nickel-selen. *Neues Jahrbuch für Mineralogie, Abhandlungen*. **1960**, *94*, 1147 – 1159. <http://www.crystallography.net/cod/9009245>.
- (38) García-García, F. J.; Larsson, A.-K.; Norèn, L.; Withers, R. L. The Crystal Structures of Co_3Se_4 and Co_7Se_8 . *Solid State Sciences* **2004**, *6* (7), 725–733. <https://doi.org/10.1016/j.solidstatesciences.2004.03.030>.
- (39) Gopinath, C. S.; Nalajala, N. A scalable and thin film approach for solar hydrogen generation: a review on enhanced photocatalytic water splitting. *J. Mater. Chem. A*, **2021**, *9*, 1353–1371. <https://doi.org/10.1039/D0TA09619A>.
- (40) Nalajala, N.; Patra, K. K.; Bharad, P. A.; Gopinath, C. S. Why the thin film form of a photocatalyst is better than the particulate form for direct solar-to-hydrogen conversion: a poor man's approach. *RSC Adv.*, **2019**, *9*, 6094–6100. <https://doi.org/10.1039/C8RA09982K>.
- (41) Macrae, C. F.; Sovago, I.; Cottrell, S. J.; Galek, P. T. A.; McCabe, P.; Pidcock, E.; Platings, M.; Shields, G. P.; Stevens, J. S.; Towler, M.; Wood, P. A. Mercury 4.0 : From Visualization to Analysis, Design and Prediction. *Journal of Applied Crystallography* **2020**, *53* (1), 226–235. <https://doi.org/10.1107/S1600576719014092>.
- (42) Kaminsky, W. From CIF to Virtual Morphology Using the WinXMorph Program. *Journal of Applied Crystallography* **2007**, *40* (2), 382–385. <https://doi.org/10.1107/S0021889807003986>.
- (43) Rodríguez-Carvajal, J. Recent Advances in Magnetic Structure Determination by Neutron Powder Diffraction. *Physica B: Condensed Matter* **1993**, *192* (1–2), 55–69. [https://doi.org/10.1016/0921-4526\(93\)90108-I](https://doi.org/10.1016/0921-4526(93)90108-I).
- (44) Patterson, A. L. The Scherrer Formula for X-Ray Particle Size Determination. *Physical Review* **1939**, *56* (10), 978–982. <https://doi.org/10.1103/PhysRev.56.978>.
- (45) Cullity, B. D.; Stock, S. R. Elements of X-ray Diffraction (Book), Third Edition. *Prentice-Hall*, **2001**.
- (46) Guinier, A. Phase Transformations in Solids Edited by R. Smoluchowski, J. E. Mayer and W. A. Weyl. *Acta Crystallographica* **1952**, *5* (6), 857–858. <https://doi.org/10.1107/S0365110X52002434>.
- (47) Xie, H.; Yin, F.; Yu, T.; Wang, J.-T.; Liang, C. Mechanism for Direct Graphite-to-Diamond Phase Transition. *Scientific Reports* **2015**, *4* (1), 5930. <https://doi.org/10.1038/srep05930>.(48) Arlt, T.; Angel, R. J. Displacive Phase Transitions in C-Centred Clinopyroxenes: Spodumene, $\text{LiScSi}_2\text{O}_6$ and ZnSiO_3 . *Physics and Chemistry of Minerals* **2000**, *27* (10), 719–731. <https://doi.org/10.1007/s002690000116>.
- (49) Hoene, J. von; Charles, R. G.; Hickam, W. M. Thermal Decomposition of Metal Acetylacetonates: Mass Spectrometer Studies. *The Journal of Physical Chemistry* **1958**, *62* (9), 1098–1101. <https://doi.org/10.1021/j150567a019>.

- (50) A. Bravais. Etudes Crystallographiques. *Paris: Gauthier-Villars, 1866.*
- (51) M. G. Friedel. Etudes sur la loi de Bravais. ' *Bull. Soc. Franc. Miner.*, 9:326, **1907.**
- (52) J. D. H. Donnay and D. Harker. A new law of crystal morphology extending the law of bravais. *Amer. Min.*, 22:446, **1937.**
- (53) Hartman, P.; Perdok, W. G. On the Relations between Structure and Morphology of Crystals. I. *Acta Crystallographica* **1955**, 8 (1), 49–52. <https://doi.org/10.1107/S0365110X55000121>.
- (54) Hartman, P.; Perdok, W. G. On the Relations between Structure and Morphology of Crystals. II. *Acta Crystallographica* **1955**, 8 (9), 521–524. <https://doi.org/10.1107/S0365110X55001679>.
- (55) Hartman, P.; Perdok, W. G. On the Relations between Structure and Morphology of Crystals. III. *Acta Crystallographica* **1955**, 8 (9), 525–529. <https://doi.org/10.1107/S0365110X55001680>.
- (56) Dandekar, P.; Doherty, M. F. A Mechanistic Growth Model for Inorganic Crystals: Solid-State Interactions. *AIChE Journal* **2014**, 60 (11), 3707–3719. <https://doi.org/10.1002/aic.14597>.
- (57) Arrott, A. S. Generalized Curie-Weiss Law. *Physical Review B* **1985**, 31 (5), 2851–2856. <https://doi.org/10.1103/PhysRevB.31.2851>.
- (58) Néel, M. L. Propriétés Magnétiques Des Ferrites; Ferrimagnétisme et Antiferromagnétisme. *Annales de Physique* 1948, 12 (3). <https://doi.org/10.1051/anphys/194812030137>.
- (59) Yamanaka, T.; Okita, M. Magnetic Properties of the Fe₂SiO₄-Fe₃O₄ Spinel Solid Solutions. *Physics and Chemistry of Minerals* 2001, 28 (2), 102–109. <https://doi.org/10.1007/s002690000135>.
- (60) Goya, G. F.; Berquó, T. S.; Fonseca, F. C.; Morales, M. P. Static and Dynamic Magnetic Properties of Spherical Magnetite Nanoparticles. *Journal of Applied Physics* 2003, 94 (5), 3520–3528. <https://doi.org/10.1063/1.1599959>.
- (61) Levy, D.; Giustetto, R.; Hoser, A. Structure of Magnetite (Fe₃O₄) above the Curie Temperature: A Cation Ordering Study. *Physics and Chemistry of Minerals* 2012, 39 (2), 169–176. <https://doi.org/10.1007/s00269-011-0472-x>.
- (62) Hu, P.; Chang, T.; Chen, W. J.; Deng, J.; Li, S. L.; Zuo, Y. G.; Kang, L.; Yang, F.; Hostetter, M.; Volinsky, A. A. Temperature Effects on Magnetic Properties of Fe₃O₄ Nanoparticles Synthesized by the Sol-Gel Explosion-Assisted Method. *Journal of Alloys and Compounds* 2019, 773, 605–611. <https://doi.org/10.1016/j.jallcom.2018.09.238>.
- (63) Roth, W. L. THE MAGNETIC STRUCTURE OF Co₃O₄; *J. Phys. Chem. Solids* Pergamon Press, 1964, 25, 1-10. [https://doi.org/10.1016/0022-3697\(64\)90156-8](https://doi.org/10.1016/0022-3697(64)90156-8).
- (64) Tagaya, K.; Fukada, M. FMR Study of Nickel Oxide with Spinel-Type Defect Structure in Thin Films. *Jpn. J. Appl. Phys.* 1980, 19, 59. <https://doi.org/10.1143/JJAP.19.59>.
- (65) Katada, K.; Nakahigashi, K.; Shimomura, Y. Precipitates with a Defect Structure in Thin Film of NiO. *Jpn. J. Appl. Phys.* 1970, 9, 1019. <https://doi.org/10.1143/JJAP.9.1019>.

- (66) Buckett, M. I.; Marks, L. D. Formation of a Ni₃O₄ Spinel Phase on the Surface of NiO during Electron Irradiation. *MRS Online Proceedings Library* 1988, 129, 521–526. <https://doi.org/10.1557/PROC-129-521>.
- (67) Tagaya, K.; Fukada, M. Ferrimagnetism of Precipitates with a Defect Structure of Spinel-Type in Thin Film of NiO. *Jpn. J. Appl. Phys.* 1976, 15, 561. <https://doi.org/10.1143/JJAP.15.561>.
- (68) Tagaya, K. Exchange Anisotropy of Ferrimagnetic Precipitates of Nickel Oxide in NiO Matrix. *J. Phys. Soc. Jpn.* 1981, 50, 2533-2538. <https://doi.org/10.1143/JPSJ.50.2533>.
- (69) Roberts, A. P.; Chang, L.; Rowan, C. J.; Horng, C. S.; Florindo, F. Magnetic Properties of Sedimentary Greigite (Fe₃S₄): An Update. *Reviews of Geophysics* 2011, 49, 1. <https://doi.org/10.1029/2010RG000336>.
- (70) Wang, J.; Cao, S. H.; Wu, W.; Zhao, G. M. The Curie Temperature and Magnetic Exchange Energy in Half-Metallic Greigite Fe₃S₄. *Physica Scripta* 2011, 83, 4. <https://doi.org/10.1088/0031-8949/83/04/045702>.
- (71) Spender, M. R.; Coey, J. M. D.; Morrish, A. H. The Magnetic Properties and Mossbauer Spectra of Synthetic Samples of Fe₃S₄. *Canadian Journal of Physics* 1972, 50, 19. <https://doi.org/10.1139/p72-306>.
- (72) Braga, M.; Lie, S. K.; Taft, C. A.; Lester, W. A. Electronic Structure, Hyperfine Interactions, and Magnetic Properties for Iron Octahedral Sulfides. *Phys Rev B Condens Matter.* 1988, 38, 10837-10851. <https://doi.org/10.1103/PhysRevB.38.10837>.
- (73) Chang, L.; Rainford, B. D.; Stewart, J. R.; Ritter, C.; Roberts, A. P.; Tang, Y.; Chen, Q. Magnetic Structure of Greigite (Fe₃S₄) Probed by Neutron Powder Diffraction and Polarized Neutron Diffraction. *Journal of Geophysical Research: Solid Earth.* 2009, 114, 07101. <https://doi.org/10.1029/2008JB006260>.
- (74) Coey, J. M. D.; Spender, M. R.; Morrish, A. H. THE MAGNETIC STRUCTURE OF THE SPINEL Fe₃S₄. *Solid State Communications.* 1970, 8, 1605-1608. [https://doi.org/10.1016/0038-1098\(70\)90473-4](https://doi.org/10.1016/0038-1098(70)90473-4).
- (75) Heidelberg, R. F.; Luxem, A.H.; Talhouk, S.; Banewicz, J. J. The Magnetic Susceptibilities of the Cobalt-Sulfur System. *Inorg. Chem.* 1966, 5, 194–197. <https://doi.org/10.1021/ic50036a007>.
- (76) Miyazaki, S.; Shirai, M.; Suzuki, N. Electronic band structure of antiferromagnetic spinel Co₃S₄. *Journal of Magnetism and Magnetic Materials.* 1998, 177-181, 1367-1368. [https://doi.org/10.1016/S0304-8853\(97\)00472-1](https://doi.org/10.1016/S0304-8853(97)00472-1).
- (77) Nishihara, H.; Kanomata, T.; Kaneko, T.; Yasuoka, H. Pulsed Nuclear Magnetic Resonance of ⁵⁹Co in Co₃S₄. *Journal of Applied Physics* 1991, 69, 4618. <https://doi.org/10.1063/1.348331>.
- (78) Jeong, Y. U.; Manthiram, A. Synthesis of Nickel Sulfides in Aqueous Solutions Using Sodium Dithionite. *Inorganic Chemistry* 2001, 40, 73–77. <https://doi.org/10.1021/ic000819d>.
- (79) Manthiram, A.; Jeong, Y. U. Ambient Temperature Synthesis of Spinel Ni₃S₄: An Itinerant Electron Ferrimagnet. *Journal of Solid State Chemistry*, 1999, 147, 679-681. <https://doi.org/10.1006/jssc.1999.8492>.

- (80) Andresen, A. F. A Neutron Diffraction Investigation of Fe₃Se₄. *Acta Chemica Scandinavica* **1968**, *22*, 827-835. [10.3891/acta.chem.scand.22-0827](https://doi.org/10.3891/acta.chem.scand.22-0827).
- (81) Cullity, B. D.; Graham, C. D. *Introduction to Magnetic Materials*, Second Edition. **2008**, 9780471477419. DOI:10.1002/9780470386323.
- (82) Li, P.; Xia, C.; Zhang, Q.; Guo, Z.; Cui, W.; Bai, H.; Alshareef, H. N.; Zhang, X. Fabrication and Characterization of Nanostructured Fe₃S₄, an Isostructural Compound of Half-Metallic Fe₃O₄. *Journal of Applied Physics* **2015**, *117* (22), 223903. <https://doi.org/10.1063/1.4922578>.
- (83) Chang, L.; Roberts, A. P.; Tang, Y.; Rainford, B. D.; Muxworthy, A. R.; Chen, Q. Fundamental Magnetic Parameters from Pure Synthetic Greigite (Fe₃S₄). *Journal of Geophysical Research* **2008**, *113* (B6), B06104. <https://doi.org/10.1029/2007JB005502>.
- (84) Wu, M.; Tse, J. S.; Pan, Y. Electronic Structures of Greigite (Fe₃S₄): A Hybrid Functional Study and Prediction for a Verwey Transition. *Scientific Reports* **2016**, *6* (1), 21637. <https://doi.org/10.1038/srep21637>.
- (85) Verwey, E. J.; Haayman, P. W.; Romeijn, F. C. Physical Properties and Cation Arrangement of Oxides with Spinel Structures II. Electronic Conductivity. *The Journal of Chemical Physics* **1947**, *15* (4), 181–187. <https://doi.org/10.1063/1.1746466>.
- (86) Thota, S.; Singh, S. Nature of Magnetic Ordering in Cobalt-Based Spinel. In *Magnetic Spinel - Synthesis, Properties and Applications*; InTech, 2017. <https://doi.org/10.5772/65913>.
- (87) Schliesser, J. M.; Huang, B.; Sahu, S. K.; Asplund, M.; Navrotsky, A.; Woodfield, B. F. Experimental Heat Capacities, Excess Entropies, and Magnetic Properties of Bulk and Nano Fe₃O₄-Co₃O₄ and Fe₃O₄-Mn₃O₄ Spinel Solid Solutions. *Journal of Solid State Chemistry* **2018**, *259*, 79–90. <https://doi.org/10.1016/j.jssc.2018.01.007>.
- (88) Gawali, S. R.; Gandhi, A. C.; Gaikwad, S. S.; Pant, J.; Chan, T.-S.; Cheng, C.-L.; Ma, Y.-R.; Wu, S. Y. Role of Cobalt Cations in Short Range Antiferromagnetic Co₃O₄ Nanoparticles: A Thermal Treatment Approach to Affecting Phonon and Magnetic Properties. *Scientific Reports* **2018**, *8* (1), 249. <https://doi.org/10.1038/s41598-017-18563-9>.
- (89) Li, Z.-A.; Fontañá-Troitiño, N.; Kovács, A.; Liébana-Viñas, S.; Spasova, M.; Dunin-Borkowski, R. E.; Müller, M.; Doennig, D.; Pentcheva, R.; Farle, M.; Salgueiriño, V. Electrostatic Doping as a Source for Robust Ferromagnetism at the Interface between Antiferromagnetic Cobalt Oxides. *Scientific Reports* **2015**, *5* (1), 7997. <https://doi.org/10.1038/srep07997>.
- (90) Tauc, J. Optical properties and electronic structure of amorphous Ge and Si. *Materials Research Bulletin*, **1968**, *3* (1), 37-46. [https://doi.org/10.1016/0025-5408\(68\)90023-8](https://doi.org/10.1016/0025-5408(68)90023-8).

SUPPORTING INFORMATION

Transition Metal-Driven Variations in Structure, Magnetism, and Photocatalysis of Monoclinic M_3Se_4 ($M = Fe, Co, Ni$) Nanoparticles

Monika Ghalawat^{†,‡}, Inderjeet Chauhan^{†,‡}, Dinesh Singh^{†,‡}, Chinnakonda S.

Gopinath^{†,‡*}, Pankaj Poddar^{†,‡*}

[†]*Physical & Materials Chemistry Division, CSIR-National Chemical Laboratory, Pune 411008, India*

[‡]*Academy of Scientific and Innovative Research (AcSIR), Sector 19, Kamla Nehru Nagar,
Ghaziabad, Uttar Pradesh- 201 002, India*

Number of figures: **14**

Number of schemes: **00**

Number of tables: **04**

Crystal Habit of M_3Se_4 Compounds using BFDH and HP Model

Usually, two successful approaches—Bravais Friedel Donnay Harker¹⁻³ (BFDH) and Hartman Perdok⁴⁻⁶ (HP) have been used to predict the morphology of crystals. These models have been efficiently used to predict the crystal morphology of numerous organic and inorganic crystals such as ZnO⁷, FeOOH⁸, Nd: LaVO₄⁹, BaSO₄⁴⁻⁶, GdVO₄¹⁰, GeO₂¹¹, CaCO₃¹², triglycine sulfate¹³, benzophenone¹⁴, Pb₁₇O₈Cl₁₈¹⁵, etc. and helped in understanding the experimental morphologies. Here too, we looked at the crystal habit of M_3Se_4 compounds by using these models to explain experimental observations.

To predict the morphology of a crystal— A. Bravais¹ (1866), G. Friedel² (1907), and J.D.H. Donnay and D. Harker³ (1937) proposed the theories using crystal lattice geometry and combinedly named as BFDH model. Here, the d-spacing (interplanar spacing) and SG symmetry operations are used to simulate the crystal habit for a particular crystal. Thus, as per the BFDH model, the faces with larger d spacing and higher density will grow slower and are most energetically stable. The unit cell dimensions and SG of the related crystal structure are used to calculate the relative growth rate (RGR) and morphological significance (MI) of various planes that decide the crystal's final form. The RGR and MI of low-index planes of M_3Se_4 compounds are explained in Table S2 using the BFDH model, and the crystal habit of the corresponding compounds was estimated using the WinXmorph¹⁶ software utilizing these RGR and MI.

For Fe₃Se₄ crystal, (001) and (00-1) faces are of highest MI, followed by (-101), (10-1), (101), and (-10-1) planes. The resultant crystal habit of Fe₃Se₄ is a rod-like shape with longitudinal side— (001) and (00-1) faces strongly visible, followed by (-101), (10-1), (101), and (-10-1) planes. The other planes ((011), (0-11), (01-1), (0-1-1), (110), (-110), (1-10), (-1-10)) are on the edges of the rod as shown in Figure S2a.

Further, the Co₃Se₄ crystallographic crystal habit is predicted. This compound is unlike Fe₃Se₄ because it has a distinct unit cell parameter and SG; hence its crystallographic morphology will also be different. The predicted morphology is shown in Figure S2b. The crystal habit of Co₃Se₄ is a rectangular box-like shape with longitudinal side— (100) and (-100) faces strongly visible, followed by (-201), (20-1) (001), and (00-1) planes. The other planes (110), (-110), (-1-10), (1-10) (1-1-1), (-1-11), (11-1), and (-111) are on the edges.

Since Ni₃Se₄ and Fe₃Se₄ have almost identical crystal properties, their crystallographic morphologies are likewise similar (as shown Figure S2c).

This model, however, has ignored one of the most essential factors in determining the crystal's morphology— bond energies and their orientations present in the crystal system. Therefore, it is crucial to discuss the proper consideration of several interaction energies present between the crystallizing entities in M_3Se_4 compounds.

In 1955, P. Hartman and W.G. Perdok⁴⁻⁶ developed a model based on bond energies to predict any crystal's morphology. They demonstrated that the periodic chains of strong bonds present in the internal crystal structure play an essential role in deciding the crystal's final morphology. All the crystal faces are divided into three parts depending on the periodic chains of strong bonds named as PBC (periodic bond chain) vectors— F: flat faces (parallel to two PBC vectors), S: stepped faces (parallel to only one PBC vector), and K: kinked faces (not parallel to any PBC vector). The sequence of MI faces for appearance in the final crystal habit is $F > S > K$. Further, to predict the crystal morphology using this model, the inversion symmetry operator should be present. As if the inversion operator is not present, an intrinsic dipole moment is present within the unit cell, and this model works only for crystals with non-polar unit cells. The list of symmetry operators of M_3Se_4 is discussed in Figure S3. Given that all M_3Se_4 compounds contain the inversion operator, the HP model can be used to predict the crystal habit of these phases.

Figure S4 to S6 show the packing diagram of M_3Se_4 crystal having a blue cloud shape PBC vector. PBC vector completely lies on the (010) and (0-10) planes of the M_3Se_4 structure. Accordingly, these planes are in the F category of faces and are most visible in the final crystal shape in all three compounds. In case of Fe_3Se_4 and Ni_3Se_4 , large component of PBC vectors lie on the (001), (00-1), (101), (-101), (10-1), (-10-1), (110), (-110), (1-10), (-1-10), (011), (0-11), (01-1), (0-1-1), (111), (-1-1-1), (-111), (1-11), (11-1), (1-1-1), (-11-1), and (-1-11) planes. While, in Co_3Se_4 , large component of PBC vectors lie on the (100), (-100), (-201), (20-1), (101), (-10-1), (10-1), (-101), (110), (-110), (1-10), (-1-10), (011), (01-1), (0-11), (0-1-1), (111), (-1-1-1), (-111), (1-11), (11-1), (1-1-1), (-11-1), (1-1-1) planes. Therefore, these planes correspond to the S category of faces for the corresponding samples. In the case of Fe_3Se_4 and Ni_3Se_4 , the (100) and (-100) planes are not parallel to any PBC vector, while, in Co_3Se_4 , they are (001), (00-1) planes. Therefore, they belong to the K category having the least visibility in the final morphology. A table summarizing all M_3Se_4 crystal planes of different categories based on the HP model is Table S3— which provides the RGR and MI for distinct faces of corresponding M_3Se_4 compounds. Again, the WinXmorph¹⁶ software has been used to estimate the crystal habit of M_3Se_4 compounds using these RGR and MI. It is observed that the (010)

and (0-10) faces are of the highest MI for all M_3Se_4 crystals. In Figure S7, the morphological drawing predicted using HP theory illustrates the resultant crystal habit as a hexagonal-cylindrical-like shape with two enormously visible upper planes (010) and (0-10). It is noted that in all the M_3Se_4 compounds, the predicted crystal habit using the HP model is nearly the same with slight variation in Co_3Se_4 as bonding is nearly identical in all compounds.

Table S1. Rietveld refinement data of the as-synthesized M_3Se_4 nanoparticles — Fe_3Se_4 , Co_3Se_4 , and Ni_3Se_4 . The parameters χ^2 represented the squared ratio between R-factor from the refinement and R-factor expected from counting statistics, and wR_p (%) is the weighted profile R-value. Unit cell parameters are denoted by a, b, c, α , β , and γ .¹⁷

Compound Parameter	Fe_3Se_4	Co_3Se_4	Ni_3Se_4
χ^2	1.69	15.2	24.8
wR_p (%)	25.9	28.2	20.3
Space group	I2/m	C2/m	I2/m
Structure	Monoclinic	Monoclinic	Monoclinic
a (Å)	6.2	12.2	6.2
b (Å)	3.5	3.5	3.6
c (Å)	11.3	6.2	10.5
α	90°	90°	90°
β	91.8°	121.8°	90.7°
γ	90°	90°	90°

Table S2. Morphological importance of several faces of M_3Se_4 crystals (Fe_3Se_4 , Co_3Se_4 , and Ni_3Se_4) based on the Bravais-Friedel-Donnay-Harker (BFDH) model. The d_{hkl} represents the interplanar spacing in Å. RGR and MI are calculated as ‘relative growth rates’ and ‘morphological importance’, respectively.

Phase	Faces (hkl)	d_{hkl} (Å)	RGR	MI
Fe_3Se_4	(001), (00 $\bar{1}$)	11.27	1	1
	($\bar{1}01$), (10 $\bar{1}$)	5.51	2.04	0.49
	(101), ($\bar{1}0\bar{1}$)	5.36	2.10	0.48
	(011), (0 $\bar{1}1$), (0 $\bar{1}\bar{1}$), (01 $\bar{1}$)	3.37	3.34	0.29
	(110), ($\bar{1}10$), ($\bar{1}\bar{1}0$), (1 $\bar{1}0$)	3.07	3.66	0.27
Co_3Se_4	(100), ($\bar{1}00$)	10.40	1	1
	(001), (00 $\bar{1}$)	5.34	1.94	0.51
	($\bar{2}01$), (20 $\bar{1}$)	5.21	1.99	0.49
	(110), ($\bar{1}10$), ($\bar{1}\bar{1}0$), (1 $\bar{1}0$)	3.37	3.07	0.32
	(1 $\bar{1}\bar{1}$), ($\bar{1}\bar{1}1$), (11 $\bar{1}$), ($\bar{1}11$)	3.08	3.36	0.29
Ni_3Se_4	(001), (00 $\bar{1}$)	10.25	1	1
	($\bar{1}01$), (10 $\bar{1}$), (101), ($\bar{1}0\bar{1}$)	5.32	1.96	0.50
	(011), (0 $\bar{1}1$), (0 $\bar{1}\bar{1}$), (01 $\bar{1}$)	3.43	3.04	0.32
	(110), ($\bar{1}10$), ($\bar{1}\bar{1}0$), (1 $\bar{1}0$)	3.13	3.33	0.29

Table S3. Morphological importance of several faces of M_3Se_4 (Fe_3Se_4 , Co_3Se_4 , and Ni_3Se_4) crystals based on the Hartman-Perdok (HP) model. All the faces are categorized according to their alignment with PBC vectors. Here, MI stands for ‘morphological importance’.

S. No.	Faces (hkl)	PBC vectors lying parallel to (hkl) planes	Face category	MI
Fe_3Se_4 and Ni_3Se_4	(010), (0 $\bar{1}$ 0)	Blue	F	Largest
	(001), (00 $\bar{1}$), (101), ($\bar{1}$ 0 $\bar{1}$), (10 $\bar{1}$), ($\bar{1}$ 01), (110), ($\bar{1}$ $\bar{1}$ 0), (1 $\bar{1}$ 0), ($\bar{1}$ $\bar{1}$ 0), (011), (0 $\bar{1}$ 1), (01 $\bar{1}$), (0 $\bar{1}$ $\bar{1}$), (111), ($\bar{1}$ $\bar{1}$ $\bar{1}$), ($\bar{1}$ 11), (1 $\bar{1}$ 1), (11 $\bar{1}$), (1 $\bar{1}$ $\bar{1}$), ($\bar{1}$ 1 $\bar{1}$), ($\bar{1}$ $\bar{1}$ 1)	Large component of blue	S	Large
	(100), ($\bar{1}$ 00)	No PBC vector lie along these planes	K	Smallest
Co_3Se_4	(010), (0 $\bar{1}$ 0)	Blue	F	Largest
	(100), ($\bar{1}$ 00), ($\bar{2}$ 01), (20 $\bar{1}$), (101), ($\bar{1}$ 0 $\bar{1}$), (10 $\bar{1}$), ($\bar{1}$ 01), (110), ($\bar{1}$ $\bar{1}$ 0), (1 $\bar{1}$ 0), ($\bar{1}$ $\bar{1}$ 0), (011), (0 $\bar{1}$ 1), (01 $\bar{1}$), (0 $\bar{1}$ $\bar{1}$), (111), ($\bar{1}$ $\bar{1}$ $\bar{1}$), ($\bar{1}$ 11), (1 $\bar{1}$ 1), (11 $\bar{1}$), (1 $\bar{1}$ $\bar{1}$), ($\bar{1}$ 1 $\bar{1}$), ($\bar{1}$ $\bar{1}$ 1)	Large component of blue	S	Large
	(001), (00 $\bar{1}$)	No PBC vector lie along these planes	K	Smallest

Table S4. Comparison of magnetic properties of M_3X_4 compounds (where M can be Fe, Co, and Ni, and X can be O, S, and Se) with their corresponding magnetic transition temperature.

(M₃X₄)			
X \ M	Fe	Co	Ni
O	Ferrimagnetic ¹⁸⁻²² (T _C ~ 858 K)	Antiferromagnetic ²³ (T _N ~ 40 K)	Ferrimagnetic ²⁴⁻²⁸ (T _C ~ 808 K)
S	Ferrimagnetic ²⁹⁻³⁴ (T _C ~ 606 K)	Paramagnetic ³⁵ / Antiferromagnetic ^{36,37} (T _N ~ 58 K)	Ferrimagnetic ^{38,39} (T _C ~ 20 K)
Se	Ferrimagnetic ^{40,41} (T _C ~ 314 K)	Paramagnetic ⁴²	Paramagnetic ⁴²

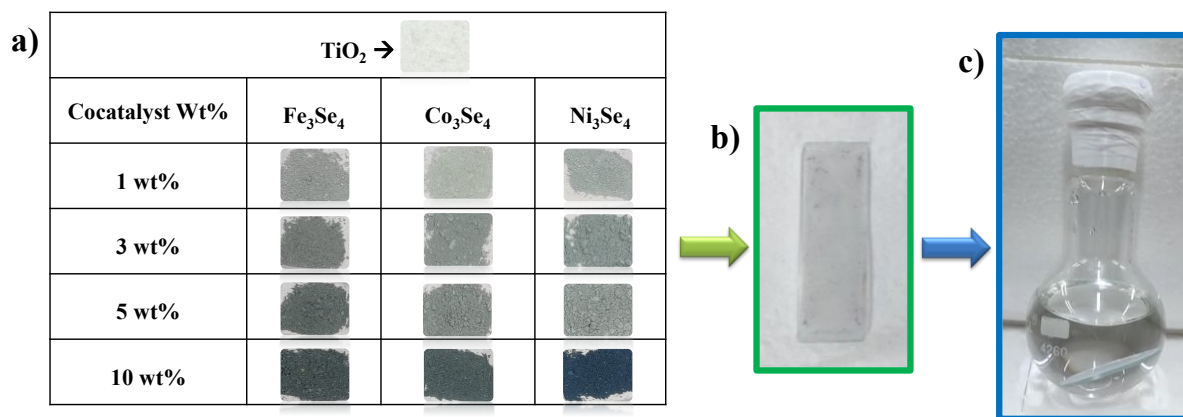


Figure S1. a) Tabulated the colour of all distinct sample, b) photographs of thin film which is used for hydrogen production using round bottom flask setup as shown in c).

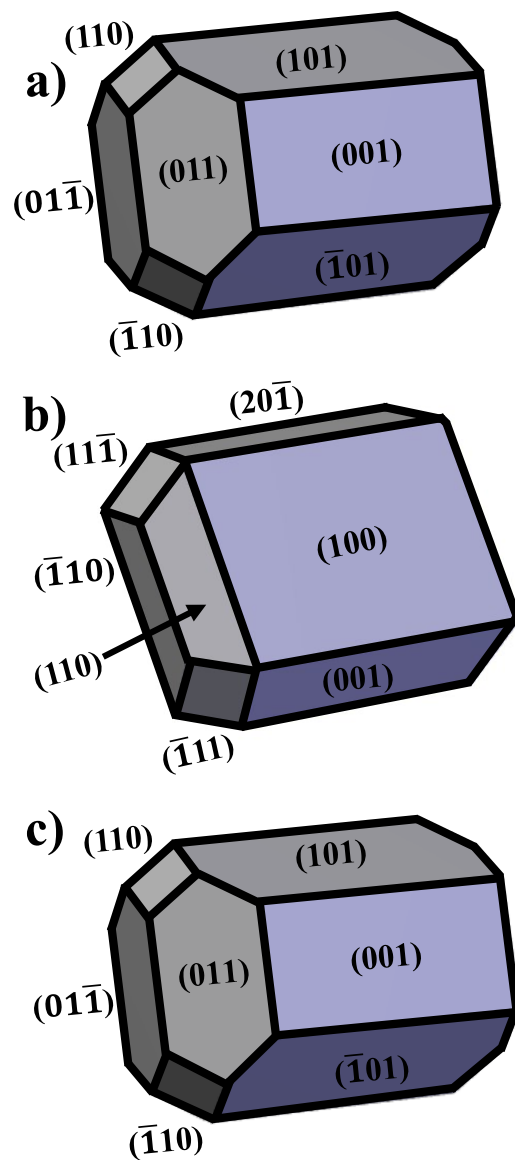


Figure S2. The predicted morphologies of M_3Se_4 crystals using Bravais-Friedel-Donnay-Harker (BFDH) model. a) Fe_3Se_4 , b) Co_3Se_4 , and c) Ni_3Se_4 show the indexed morphological drawing with corresponding hkl planes.

Fe₃Se₄		Co₃Se₄		Ni₃Se₄	
Symm. Op.	Description	Symm. Op.	Description	Symm. Op.	Description
x,y,z	Identity	x,y,z	Identity	x,y,z	Identity
-x,y,-z	Rotation axis (2-fold)	1/2+x,1/2+y,z	Centring vector	1/2+x,1/2+y,1/2+z	Centring vector
-x,-y,-z	Inversion centre ←	x,-y,z	Mirror plane	x,-y,z	Mirror plane
x,-y,z	Mirror plane	1/2+x,1/2-y,z	Glide plane	1/2+x,1/2-y,1/2+z	Glide plane
1/2+x,1/2+y,1/2+z	Centring vector	-x,y,-z	Rotation axis (2-fold)	-x,y,-z	Rotation axis (2-fold)
1/2-x,1/2+y,1/2-z	Screw axis (2-fold)	1/2-x,1/2+y,-z	Screw axis (2-fold)	1/2-x,1/2+y,1/2-z	Screw axis (2-fold)
1/2-x,1/2-y,1/2-z	Inversion centre ←	-x,-y,-z	Inversion centre ←	-x,-y,-z	Inversion centre
1/2+x,1/2-y,1/2+z	Glide plane	1/2-x,1/2-y,-z	Inversion centre ←	1/2-x,1/2-y,1/2-z	Inversion centre

Figure S3. The list of symmetry operators of M₃Se₄. a) Fe₃Se₄, b) Co₃Se₄, and c) Ni₃Se₄.

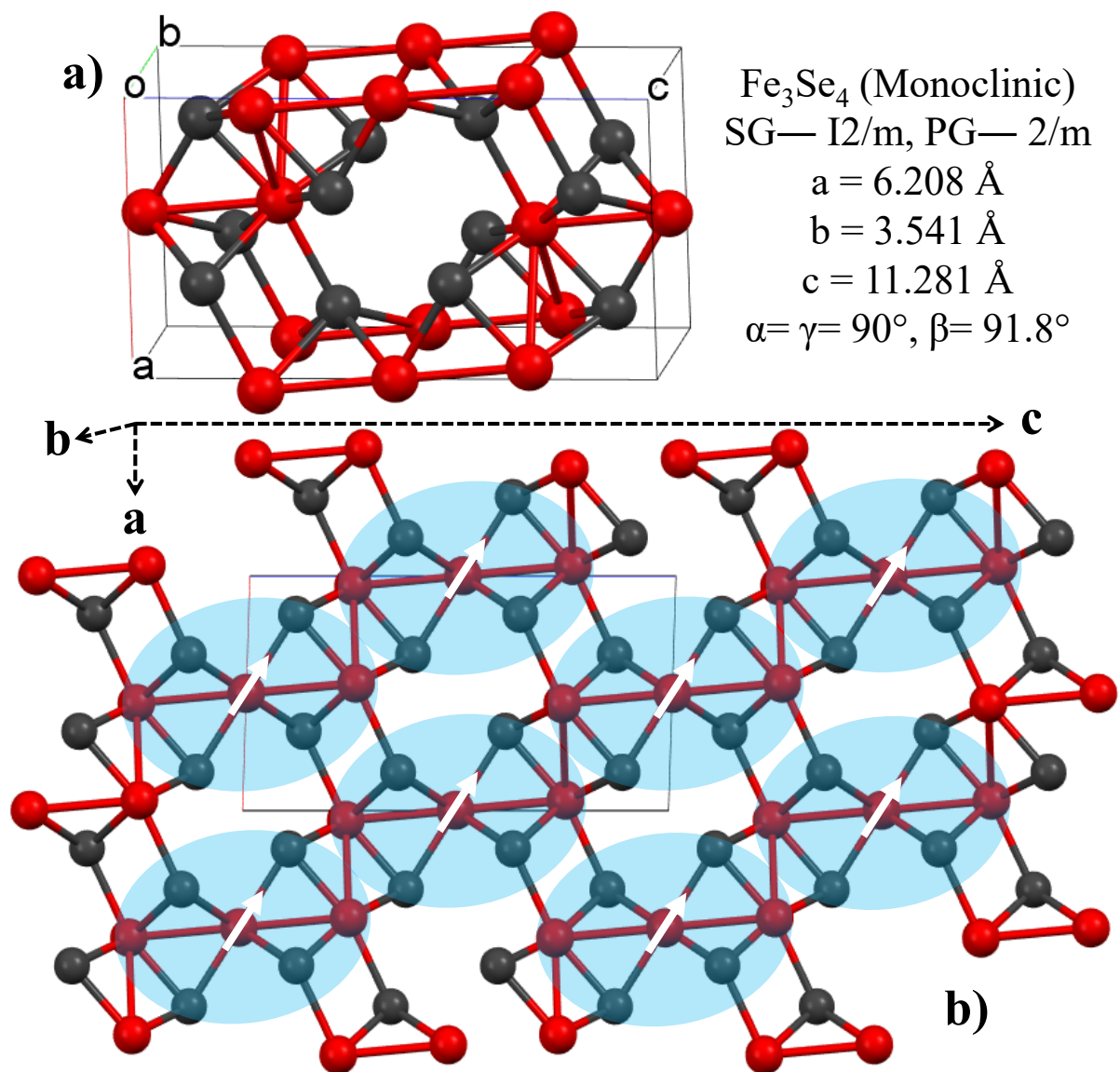


Figure S4. a) Unit cell of Fe_3Se_4 . b) Packing diagram of Fe_3Se_4 crystal along with 1 PBC vector represented by blue cloud having stoichiometry Fe_3Se_4 . The three crystallographic axes are denoted by a , b , and c .

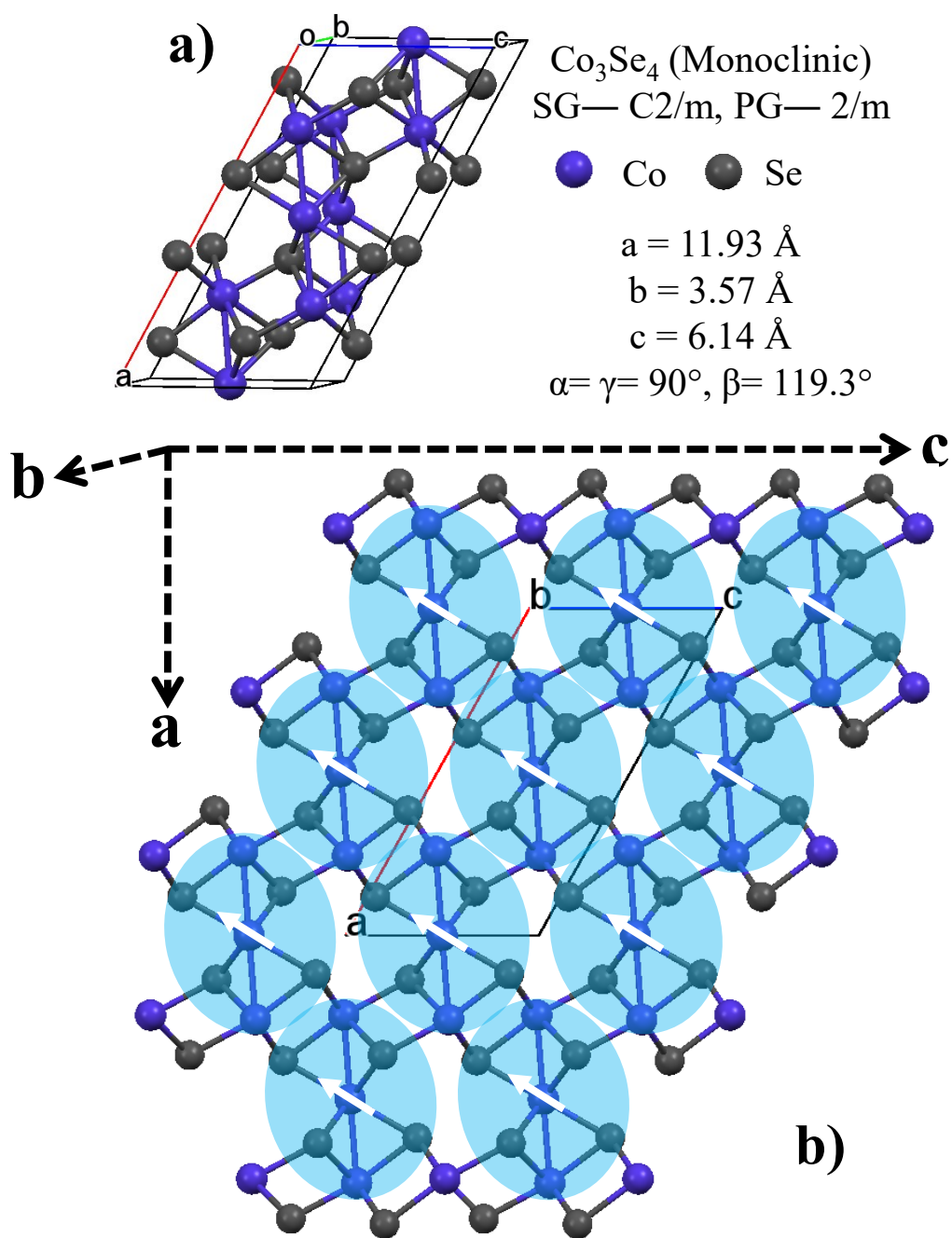


Figure S5. a) Unit cell of Co_3Se_4 . b) Packing diagram of Co_3Se_4 crystal along with 1 PBC vector represented by blue cloud having stoichiometry Co_3Se_4 . The three crystallographic axes are denoted by a, b, and c.

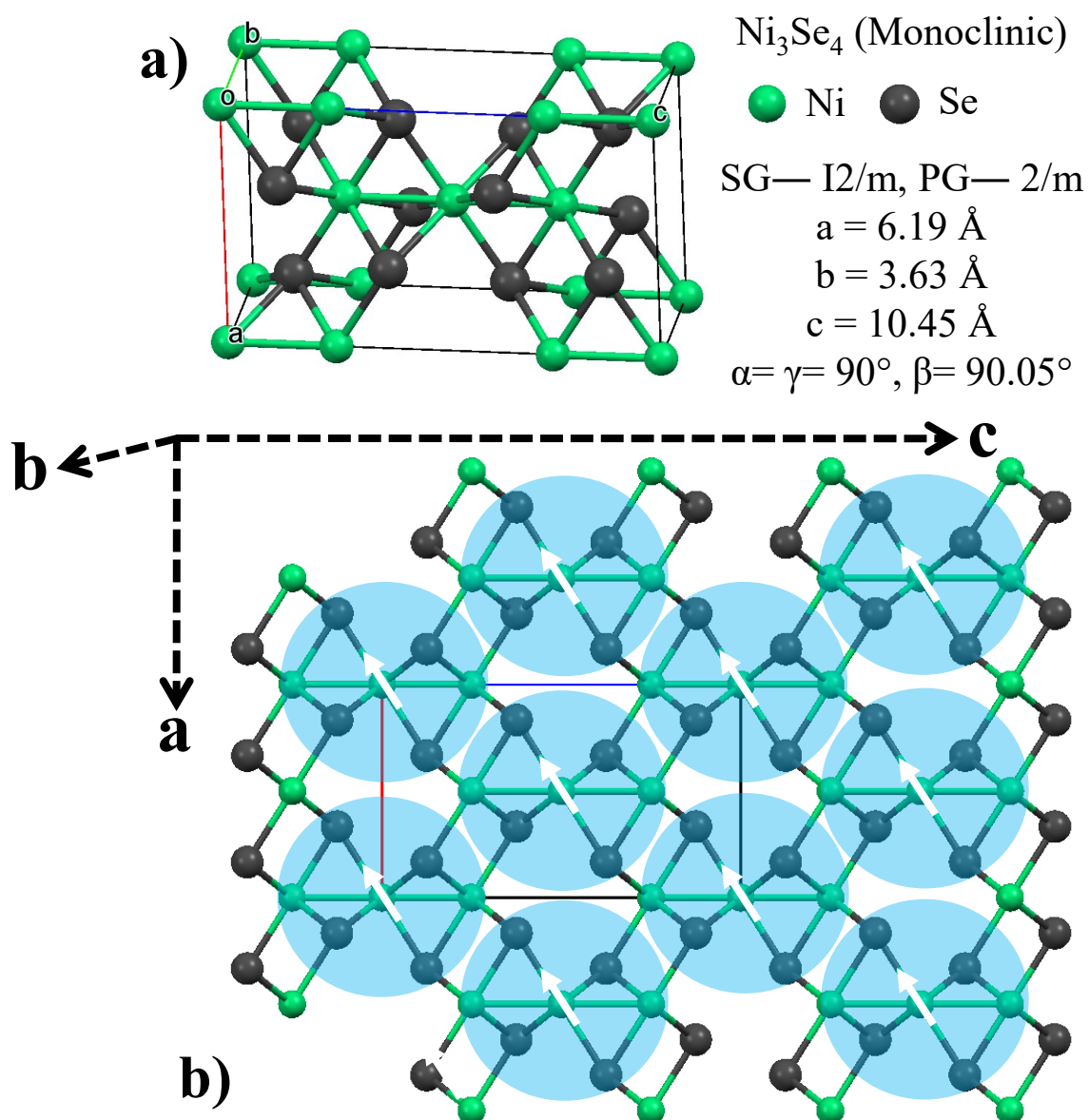


Figure S6. a) Unit cell of Ni₃Se₄. b) Packing diagram of Ni₃Se₄ crystal along with 1 PBC vector represented by blue cloud having stoichiometry Ni₃Se₄. The three crystallographic axes are denoted by a, b, and c.

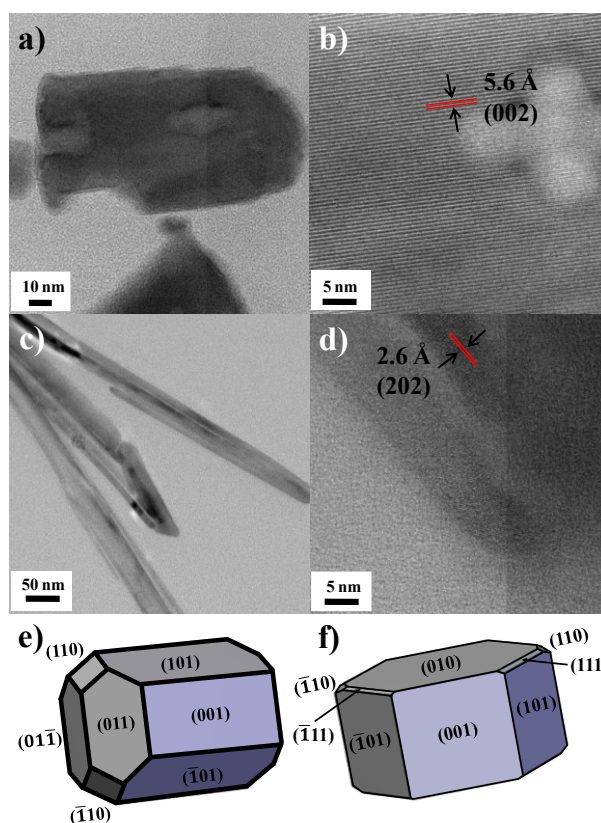


Figure S8. Correlation between the experimental and theoretically predicted morphologies of Fe₃Se₄. Figures a) and c) represent the TEM images of Fe₃Se₄ nanoparticles having the rod-like growth. Figures b) and d) show the lattice fringes spaced at 5.6 Å, and 2.6 Å representing the (002) and (202) planes of Fe₃Se₄ respectively.²⁹ Figures e) and f) represent the predicted morphology of Fe₃Se₄ by BFDH and HP model, respectively.

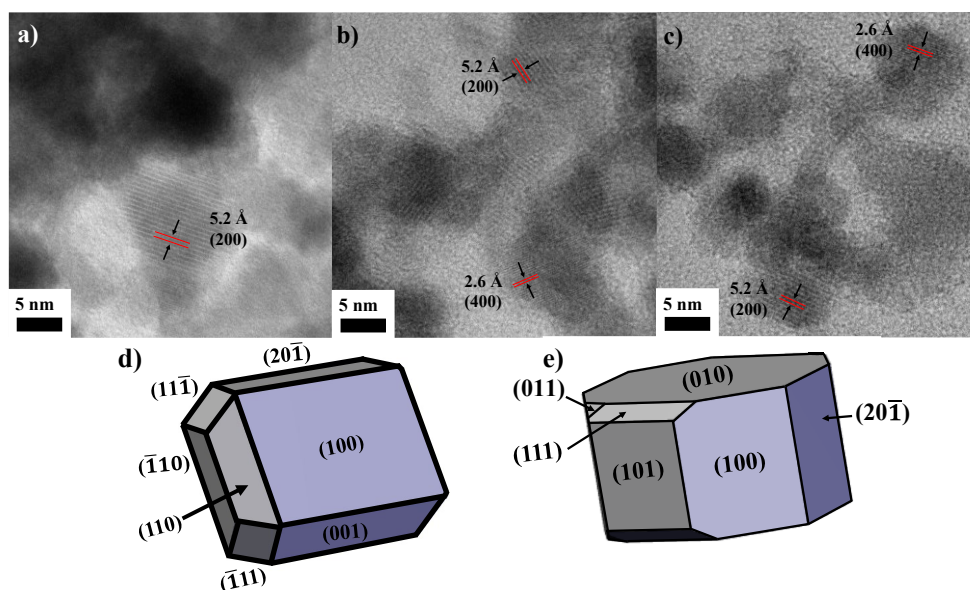


Figure S9. Correlation between experimentally-observed and theoretically-predicted morphologies of Co_3Se_4 . Figures a) to c) represent the TEM images of Co_3Se_4 nanoparticles having quasi-spherical features. Figures a), b), and c) also show the lattice fringes spaced at 5.2 Å and 2.6 Å, which represent the (200) and (400) planes of Co_3Se_4 , respectively. Figures d) and e) represent the predicted morphology of Co_3Se_4 by BFDH and HP model, respectively.

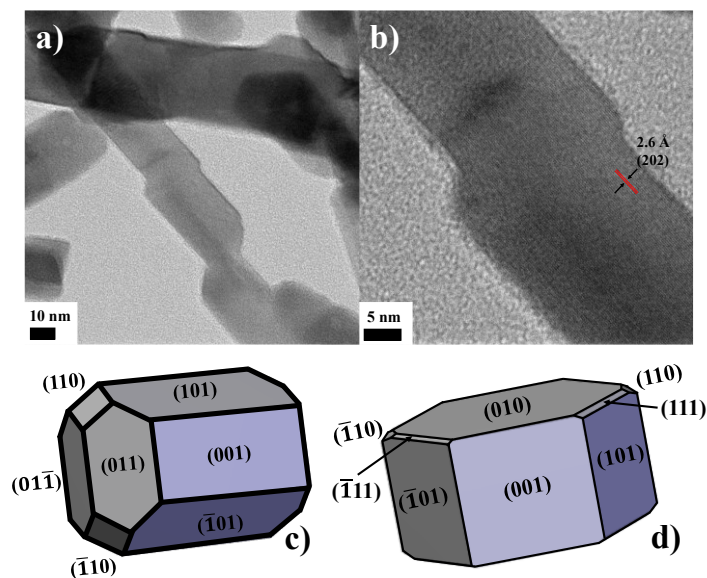


Figure S10. Correlation between the experimentally-observed and theoretically-predicted morphologies of Ni_3Se_4 . Figures a) and b) represent the TEM images of Ni_3Se_4 nanoparticles with rod-like features. Figure b) shows the lattice fringes spaced at 2.6 \AA , representing the (202) plane of Ni_3Se_4 . Figures c) and d) represent the predicted morphology of Ni_3Se_4 by BFDH and HP model, respectively.

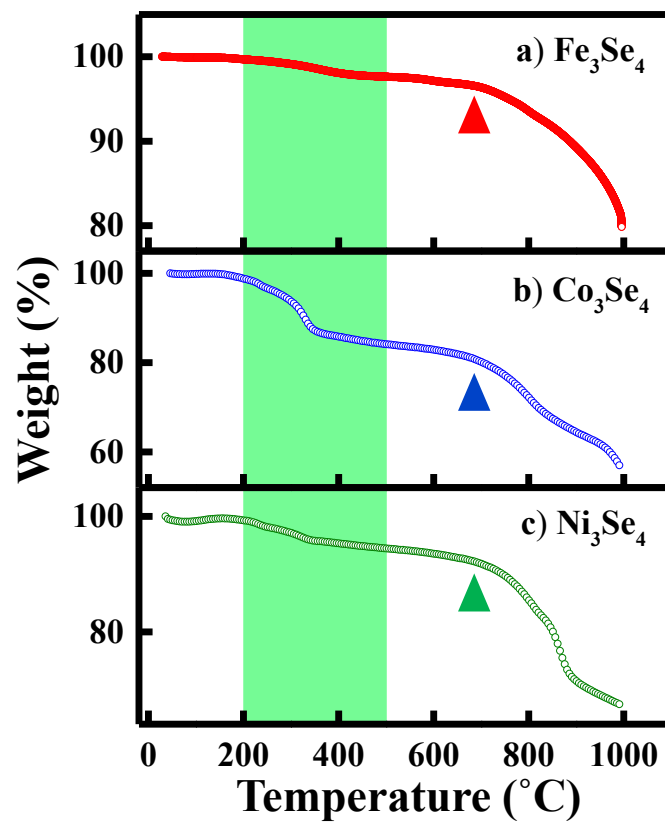


Figure S11. TGA plots of a) Fe₃Se₄²⁵ (red curve), b) Co₃Se₄ (blue curve), and c) Ni₃Se₄ (green curve). The shaded region shows the loss of organic fragments, and the triangle reveals the decomposition point in corresponding compounds.

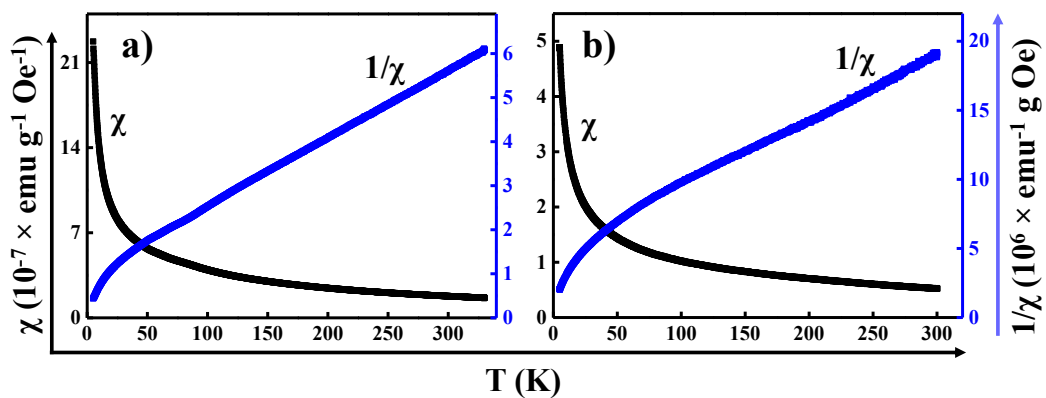


Figure S12. The black curve represents the magnetic susceptibility (χ) versus the temperature plot of a) Co_3Se_4 and b) Ni_3Se_4 , respectively, at 100 Oe. The blue curve denotes the inverse of the magnetic susceptibility versus temperature plot.

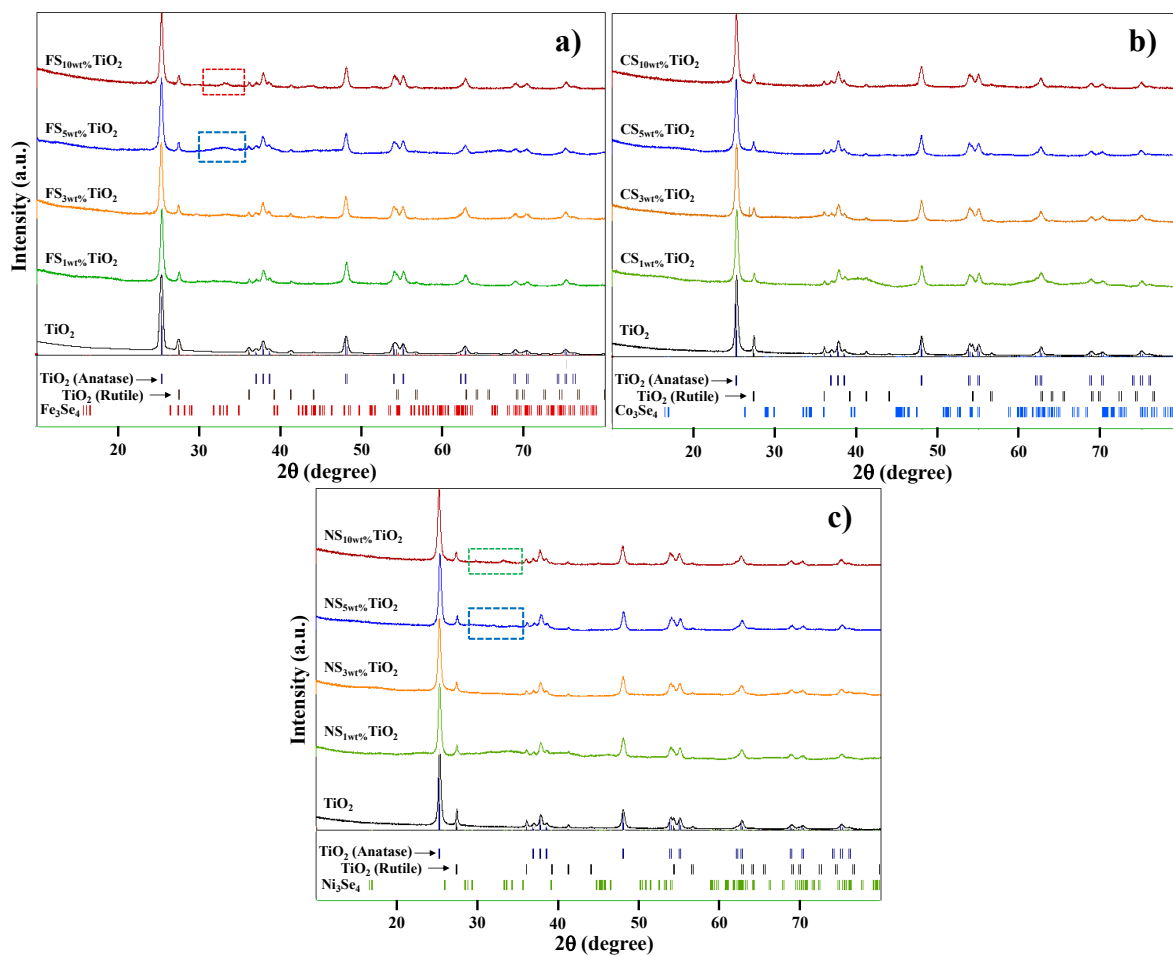


Figure S13. XRD patterns of M_3Se_4 (1 to 10 wt%)- TiO_2 with different loading amounts of M_3Se_4 .

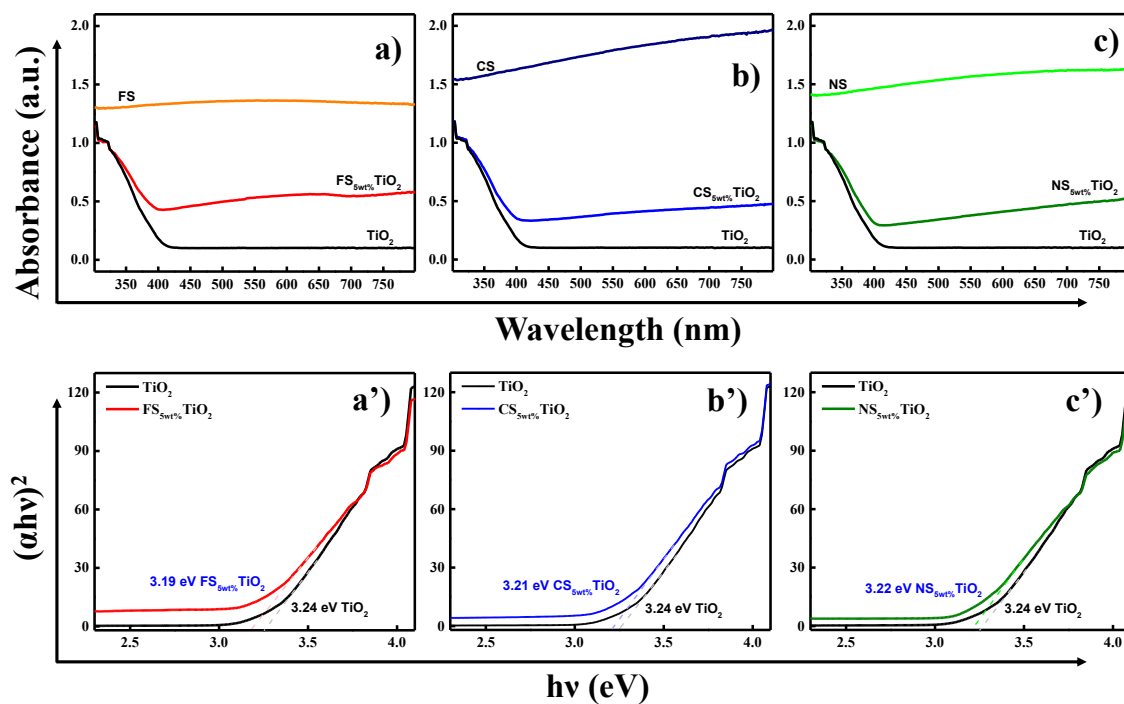


Figure S14. (a-c) UV-Visible absorption spectra of TiO₂, M₃Se₄ and M₃Se₄ (5wt%)-TiO₂; a) Fe₃Se₄ (FS), b) Co₃Se₄(CS), and c) Ni₃Se₄(NS). (b) Tauc plot of TiO₂ and M₃Se₄ (5wt%)-TiO₂; a') Fe₃Se₄ (FS) (5wt%)-TiO₂, b') Co₃Se₄ (5wt%)-TiO₂, and c') Ni₃Se₄(5wt%)-TiO₂ for their respective band gap indicated by arrows.

REFERENCES

- (1) A. Bravais. *Etudes Crystallographiques* . Paris: Gauthier-Villars, **1866**.
- (2) M. G. Friedel. *Etudes sur la loi de Bravais*. ' *Bull. Soc. Franc. Miner.*, 9:326, **1907**.
- (3) J. D. H. Donnay and D. Harker. A new law of crystal morphology extending the law of bravais. *Amer. Min.*, 22:446, **1937**.
- (4) Hartman, P.; Perdok, W. G. On the Relations between Structure and Morphology of Crystals. I. *Acta Crystallographica* **1955**, 8 (1), 49–52. <https://doi.org/10.1107/S0365110X55000121>..
- (5) Hartman, P.; Perdok, W. G. On the Relations between Structure and Morphology of Crystals. II. *Acta Crystallographica* **1955**, 8 (9), 521–524. <https://doi.org/10.1107/S0365110X55001679>.
- (6) Hartman, P.; Perdok, W. G. On the Relations between Structure and Morphology of Crystals. III. *Acta Crystallographica* **1955**, 8 (9), 525–529. <https://doi.org/10.1107/S0365110X55001680>.
- (7) Goel, S.; Sinha, N.; Yadav, H.; Kumar, B. On the Prediction of External Shape of ZnO Nanocrystals. *Physica E: Low-dimensional Systems and Nanostructures* **2019**, 106, 291–297. <https://doi.org/10.1016/j.physe.2018.08.014>.
- (8) Li, S.; Qin, G. W.; Zhang, Y.; Pei, W.; Zuo, L.; Esling, C. Anisotropic Growth of Iron Oxyhydroxide Nanorods and Their Photocatalytic Activity. *Advanced Engineering Materials* **2010**, 12 (10), 1082–1085. <https://doi.org/10.1002/adem.201000081>.
- (9) Cong, H.; Zhang, H.; Sun, S.; Yu, Y.; Yu, W.; Yu, H.; Zhang, J.; Wang, J.; Boughton, R. I. Morphological Study of Czochralski-Grown Lanthanide Orthovanadate Single Crystals and Implications on the Mechanism of Bulk Spiral Formation. *Journal of Applied Crystallography* **2010**, 43 (2), 308–319. <https://doi.org/10.1107/S0021889809052339>.
- (10) Andreici Eftimie, E.-L.; Avram, N. M.; Jelsch, C.; Nicolov, M. Morphology of the GdVO₄ Crystal: First-Principles Studies. *Acta Crystallographica Section B Structural Science, Crystal Engineering and Materials* **2020**, 76 (5), 749–756. <https://doi.org/10.1107/S2052520620009002>.
- (11) Wu, H. P.; Liu, J. F.; Ge, M. Y.; Niu, L.; Zeng, Y. W.; Wang, Y. W.; Lv, G. L.; Wang, L. N.; Zhang, G. Q.; Jiang, J. Z. Preparation of Monodisperse GeO₂ Nanocubes in a Reverse Micelle System. *Chemistry of Materials* **2006**, 18 (7), 1817–1820. <https://doi.org/10.1021/cm052456r>.
- (12) W. M. M. Heijnen. The morphology of gel grown calcite. *N. Jb. Miner. Mh.* **1985**, 8,357– 371.
- (13) Goel, S.; Sinha, N.; Hussain, A.; Joseph, A. J.; Yadav, H.; Kumar, B. Sunset Yellow Dyed Triglycine Sulfate Single Crystals: Enhanced Thermal, Mechanical, Optical and Di-/Piezo-/Ferro-/Pyro-Electric Properties. *Journal of Materials Science: Materials in Electronics* **2018**, 29 (16), 13449–13463. <https://doi.org/10.1007/s10854-018-9470-9>.
- (14) Roberts, K. J.; Docherty, R.; Bennema, P.; Jetten, L. A. M. J. The Importance of Considering Growth-Induced Conformational Change in Predicting the Morphology of Benzophenone.

Journal of Physics D: Applied Physics **1993**, 26 (8B), B7–B21. <https://doi.org/10.1088/0022-3727/26/8B/002>.

- (15) Zhang, H.; Zhang, M.; Pan, S.; Dong, X.; Yang, Z.; Hou, X.; Wang, Z.; Chang, K. B.; Poeppelmeier, K. R. $\text{Pb}_{17}\text{O}_8\text{Cl}_{18}$: A Promising IR Nonlinear Optical Material with Large Laser Damage Threshold Synthesized in an Open System. *J Am Chem Soc* **2015**, 137 (26), 8360–8363. <https://doi.org/10.1021/jacs.5b03986>.
- (16) Kaminsky, W. From CIF to Virtual Morphology Using the WinXMorph Program. *Journal of Applied Crystallography* **2007**, 40 (2), 382–385. <https://doi.org/10.1107/S0021889807003986>.
- (17) Ghalawat, M.; Poddar, P. Study of Growth Kinetics of Fe_3Se_4 Nanocrystallites and the Influence of Size and Shape Tunability on Their Magnetic Properties. *Journal of Physical Chemistry C* **2021**, 125 (14), 7932–7943. <https://doi.org/10.1021/acs.jpcc.1c00389>.
- (18) Néel, M. L. Propriétés Magnétiques Des Ferrites; Ferrimagnétisme et Antiferromagnétisme. *Annales de Physique* **1948**, 12 (3). <https://doi.org/10.1051/anphys/194812030137>.
- (19) Yamanaka, T.; Okita, M. Magnetic Properties of the $\text{Fe}_2\text{SiO}_4\text{-Fe}_3\text{O}_4$ Spinel Solid Solutions. *Physics and Chemistry of Minerals* **2001**, 28 (2), 102–109. <https://doi.org/10.1007/s002690000135>.
- (20) Goya, G. F.; Berquó, T. S.; Fonseca, F. C.; Morales, M. P. Static and Dynamic Magnetic Properties of Spherical Magnetite Nanoparticles. *Journal of Applied Physics* **2003**, 94 (5), 3520–3528. <https://doi.org/10.1063/1.1599959>.
- (21) Levy, D.; Giustetto, R.; Hoser, A. Structure of Magnetite (Fe_3O_4) above the Curie Temperature: A Cation Ordering Study. *Physics and Chemistry of Minerals* **2012**, 39 (2), 169–176. <https://doi.org/10.1007/s00269-011-0472-x>.
- (22) Hu, P.; Chang, T.; Chen, W. J.; Deng, J.; Li, S. L.; Zuo, Y. G.; Kang, L.; Yang, F.; Hostetter, M.; Volinsky, A. A. Temperature Effects on Magnetic Properties of Fe_3O_4 Nanoparticles Synthesized by the Sol-Gel Explosion-Assisted Method. *Journal of Alloys and Compounds* **2019**, 773, 605–611. <https://doi.org/10.1016/j.jallcom.2018.09.238>.
- (23) Roth, W. L. THE MAGNETIC STRUCTURE OF Co_3O_4 ; *J. Phys. Chem. Solids Pergamon Press*, **1964**, 25, 1-10. [https://doi.org/10.1016/0022-3697\(64\)90156-8](https://doi.org/10.1016/0022-3697(64)90156-8).
- (24) Tagaya, K.; Fukada, M. FMR Study of Nickel Oxide with Spinel-Type Defect Structure in Thin Films. *Jpn. J. Appl. Phys.* **1980**, 19, 59. <https://doi.org/10.1143/JJAP.19.59>.
- (25) Katada, K.; Nakahigashi, K.; Shimomura, Y. Precipitates with a Defect Structure in Thin Film of NiO. *Jpn. J. Appl. Phys.* **1970**, 9, 1019. <https://doi.org/10.1143/JJAP.9.1019>.
- (26) Buckett, M. I.; Marks, L. D. Formation of a Ni_3O_4 Spinel Phase on the Surface of NiO during Electron Irradiation. *MRS Online Proceedings Library* **1988**, 129, 521–526. <https://doi.org/10.1557/PROC-129-521>.
- (27) Tagaya, K.; Fukada, M. Ferrimagnetism of Precipitates with a Defect Structure of Spinel-Type in Thin Film of NiO. *Jpn. J. Appl. Phys.* **1976**, 15, 561. <https://doi.org/10.1143/JJAP.15.561>.

- (28) Tagaya, K. Exchange Anisotropy of Ferrimagnetic Precipitates of Nickel Oxide in NiO Matrix. *J. Phys. Soc. Jpn.* **1981**, *50*, 2533-2538. <https://doi.org/10.1143/JPSJ.50.2533>.
- (29) Roberts, A. P.; Chang, L.; Rowan, C. J.; Horng, C. S.; Florindo, F. Magnetic Properties of Sedimentary Greigite (Fe_3S_4): An Update. *Reviews of Geophysics* **2011**, *49*, 1. <https://doi.org/10.1029/2010RG000336>.
- (30) Wang, J.; Cao, S. H.; Wu, W.; Zhao, G. M. The Curie Temperature and Magnetic Exchange Energy in Half-Metallic Greigite Fe_3S_4 . *Physica Scripta* **2011**, *83*, 4. <https://doi.org/10.1088/0031-8949/83/04/045702>.
- (31) Spender, M. R.; Coey, J. M. D.; Morrish, A. H. The Magnetic Properties and Mossbauer Spectra of Synthetic Samples of Fe_3S_4 . *Canadian Journal of Physics* **1972**, *50*, 19. <https://doi.org/10.1139/p72-306>.
- (32) Braga, M.; Lie, S. K.; Taft, C. A.; Lester, W. A. Electronic Structure, Hyperfine Interactions, and Magnetic Properties for Iron Octahedral Sulfides. *Phys Rev B Condens Matter*. **1988**, *38*, 10837-10851. doi: 10.1103/physrevb.38.10837.
- (33) Chang, L.; Rainford, B. D.; Stewart, J. R.; Ritter, C.; Roberts, A. P.; Tang, Y.; Chen, Q. Magnetic Structure of Greigite (Fe_3S_4) Probed by Neutron Powder Diffraction and Polarized Neutron Diffraction. *Journal of Geophysical Research: Solid Earth*. **2009**, *114*, 07101. <https://doi.org/10.1029/2008JB006260>.
- (34) Coey, J. M. D.; Spender, M. R.; Morrish, A. H. THE MAGNETIC STRUCTURE OF THE SPINEL Fe_3S_4 . *Solid State Communications*. **1970**, *8*, 1605-1608. [https://doi.org/10.1016/0038-1098\(70\)90473-4](https://doi.org/10.1016/0038-1098(70)90473-4).
- (35) Heidelberg, R. F.; Luxem, A.H.; Talhouk, S.; Banewicz, J. J. The Magnetic Susceptibilities of the Cobalt-Sulfur System. *Inorg. Chem.* **1966**, *5*, 194-197. <https://doi.org/10.1021/ic50036a007>.
- (36) Miyazaki, S.; Shirai, M.; Suzuki, N. Electronic band structure of antiferromagnetic spinel Co_3S_4 . *Journal of Magnetism and Magnetic Materials*. **1998**, *177-181*, 1367-1368. [https://doi.org/10.1016/S0304-8853\(97\)00472-1](https://doi.org/10.1016/S0304-8853(97)00472-1).
- (37) Nishihara, H.; Kanomata, T.; Kaneko, T.; Yasuoka, H. Pulsed Nuclear Magnetic Resonance of ^{59}Co in Co_3S_4 . *Journal of Applied Physics* **1991**, *69*, 4618. <https://doi.org/10.1063/1.348331>.
- (38) Jeong, Y. U.; Manthiram, A. Synthesis of Nickel Sulfides in Aqueous Solutions Using Sodium Dithionite. *Inorganic Chemistry* **2001**, *40*, 73-77. <https://doi.org/10.1021/ic000819d>.
- (39) Manthiram, A.; Jeong, Y. U. Ambient Temperature Synthesis of Spinel Ni_3S_4 : An Itinerant Electron Ferrimagnet. *Journal of Solid State Chemistry*, **1999**, *147*, 679-681. <https://doi.org/10.1006/jssc.1999.8492>.
- (40) Andresen, A. F. A Neutron Diffraction Investigation of Fe_3Se_4 . *Acta Chemica Scandinavica* **1968**, *22*, 827-835. DOI: 10.3891/acta.chem.scand.22-0827.
- (41) Zhang, H.; Long, G.; Li, D.; Sabirianov, R.; Zeng, H. Fe_3Se_4 Nanostructures with Giant Coercivity Synthesized by Solution Chemistry. *Chemistry of Materials* **2011**, *23*, 3769-3774. <https://doi.org/10.1021/cm201610k>.

- (42) Hayashi, A.; Imada, K.; Inoue, K.; Ueda, Y.; Kosuge, K. Phase Diagram of $(M'_xM_{1-x})_3\text{Se}_4$ ($0 \leq x \leq 1$) (M, M' = 3d-Transition Metal) *Bull. Inst. Chem. Res., Kyoto Univ.*, **1986**, *64*, 4. <http://hdl.handle.net/2433/77161>.